THE JOURNAL OF PHYSICAL CHEMISTRY B

Article

Cite This: J. Phys. Chem. B XXXX, XXX, XXX−XXX

pubs.acs.org/JPCB

Structure and Physicochemical Properties of the Aβ42 Tetramer: Multiscale Molecular Dynamics Simulations

Hoang Linh Nguyen,[†,∥] Pawel Krupa,[‡] Nguyen Minh Hai,[§] Huynh Quang Linh,[∥] and Mai Suan Li*[,‡]

[†]Institute for Computational Science and Technology, SBI Building, Quang Trung Software City, Tan Chanh Hiep Ward, District 12, Ho Chi Minh City 700000, Vietnam

[‡]Institute of Physics Polish Academy of Sciences, Al. Lotników 32/46, 02-668 Warsaw, Poland

[§]Faculty of Physics and Engineering Physics, University of Science-VNU HCM, Ho Chi Minh City 700000, Vietnam

[∥]Biomedical Engineering Department, Ho Chi Minh City University of Technology-VNU HCM, 268 Ly Thuong Kiet Street, Distr. 10, Ho Chi Minh City 700000, Vietnam

Supporting Information

ABSTRACT: Despite years of intensive research, little is known about oligomeric structures present during Alzheimer's disease (AD). Excess of amyloid beta (Aβ) peptides and their aggregation are the basis of the amyloid cascade hypothesis, which attempts to explain the causes of AD. Because of the intrinsically disordered nature of Aβ monomers and the high aggregation rate of oligomers, their structures are almost impossible to resolve using experimental methods. For this reason, we used a physics-based coarse-grained force field to extensively search for the conformational space of the Aβ42 tetramer, which is believed to be the smallest stable Aβ oligomer and the most toxic one. The resulting structures were subsequently optimized, tested for stability, and compared with the proposed experimental fibril models, using molecular dynamics simulations in two popular all-atom force fields. Our results show that the Aβ42 tetramer can form polymorphic stable structures, which may explain different pathways of Aβ aggregation. The models obtained comprise the outer and core chains and, therefore, are significantly different from the structure of mature fibrils. We found that interaction with water is the reason why the tetramer is more compact and less dry inside than fibrils. Physicochemical properties of the proposed all-atom structures are consistent with the available experimental observations and theoretical expectations. Therefore, we provide possible models for further study and design of higher order oligomers.

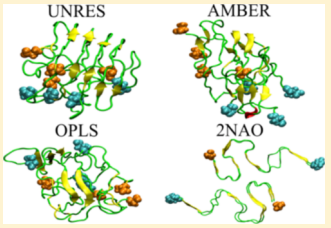

1. INTRODUCTION

Alzheimer's disease (AD) is the most prevalent type of dementia among senior population.[1] The pathological hallmarks of AD are characterized by extracellular senile plaques composed of amyloid fibrils, intracellular tangles constituted by hyperphosphorylated tau protein, neuron and synapse loss, and progression of cognitive decline.[2] Although AD has been identified more than 100 years ago, the mechanism of AD is still largely unknown. There are three main hypotheses proposed to explain the mechanism of AD including the cholinergic, tau, and amyloid cascade hypothesis.[3] It has been observed that the exaggerated aggregation of amyloid beta (Aβ) occurs before the accumulation of the hyperphosphorylated tau protein.[4−6] Based on these observations, one has proposed the amyloid cascade hypothesis, which posits that the extracellular deposit of Aβ is the cause of AD.

Extracellular plaques consist of Aβ peptides which are generated from the proteolytic cleavage of amyloid precursor protein by β- and γ-secretases.[7] Aβ has many alloforms with a length from 39 to 43 amino-acid residues. From these alloforms, $A\beta_{1-40}$ and $A\beta_{1-42}$ are the most prevalent, with 40 and 42 residues, respectively.[8] Although $A\beta_{1-40}$ is approximately 10-fold more abundant, $A\beta_{1-42}$ is the main constituent of senile plaques[9,10] as it has higher aggregation propensity and consequently higher toxicity.[10]

Aβ peptides belong to an intrinsically disordered protein class because they do not form a stable structure in water environment.[11,12] The aggregation forms of Aβ are divided into oligomers, protofibrils, and fibrils. Oligomers and protofibrils are considered as intermediate aggregates with a lower mass than the fibril and do not have a specific structure as the Aβ fibril.[13] Because Aβ peptides aggregate into fibrils to constitute plaques, the amyloid cascade hypothesis states that Aβ fibrils play a dominant role in AD. However, recent clinical trials have shown that removal of plaques cannot stop AD[14,15] and soluble aggregation states of Aβ, such as oligomers, are primary toxic species rather than mature fibrils.[16,17] Soluble Aβ oligomers also have a higher correlation with severity of AD.[18,19] Moreover, experiments observed that $A\beta_{1-42}$ but not $A\beta_{1-40}$ oligomers form pores in lipid bilayers leading to a loss of ionic homeostasis.[20,21] In agreement with these results, Drews and coworkers observed that the $A\beta_{1-42}$ tetramer or larger oligomers cross the neuron membrane, and calcium ions

Received: May 3, 2019
Revised: July 31, 2019
Published: July 31, 2019

DOI: 10.1021/acs.jpcb.9b04208
J. Phys. Chem. B XXXX, XXX, XXX−XXX

enter the cell.[22] Low-molecular weight oligomers (8−70 kDa) are far more bioactive than heavier oligomers (>150 kDa).[23] Because the mass of Aβ monomers is about 4 kDa, these oligomers are from a dimer to an 18-mer. The results from studies of Jana et al. and Ono et al. suggest that the Aβ tetramer may be the most toxic oligomer.[24,25] Thus, low-molecular weight Aβ oligomers are the most prominent targets to shed light on the mechanism of AD.

Because of the toxicity and the importance of self-assembly of Aβ oligomers, the determination of the molecular structure of these aggregation forms may allow one to understand the mechanism of AD as well as other diseases associated with protein misfolding.[3] Although the structures of mature Aβ fibrils are available in the literature,[26−30] the structure of soluble Aβ oligomers is still largely unknown. Experiments show that Aβ fibrils are in the "cross-beta" structure, where Aβ molecules assemble into β-sheets with β-strands aligned perpendicularly to the long axis of the fibril.[31] The relative arrangements of monomers in the cross section of the fibril lead to the polymorphic character of the Aβ fibril.[31] Aβ fibrils favor in-register parallel β-sheets except fibrils formed by the Iowa mutation.[32,33] In contrast to fibrils, experiments show that Aβ oligomers and protofibrils are still in a disordered structure, and the β-content generally increases with the increase of their molecular weight.[3] The oligomers can form both antiparallel and parallel β-sheet structures.[34,35] These results suggest that oligomers and protofibrils undergo structural rearrangement to form fibrils. However, Qiang and coworkers observed that $A\beta_{1-40}$ protofibrils with the antiparallel structure of the Iowa mutation are metastable and dissociated to monomers before assembling to fibrils with a parallel structure.[33] Therefore, these reports indicate that oligomers and protofibrils are polymorphic and that an antiparallel structure can be off-pathway to fibril formation.

As experiments only determine a general characteristic of oligomer structures, the molecular dynamics (MD) technique is a tool that can provide key insights into the structure of oligomers. Simulations using replica exchange and classical MD for Aβ monomers, dimers, and their mutants are usually consistent with the experimental data.[36−48] However, simulations for higher weight Aβ oligomers are difficult to conduct because of the very large number of degrees of freedom and the fact that initial structures can bias toward specific conformations. Brown and coworkers simulated the $A\beta_{42}$ tetramer and its interactions with the lipid membrane.[49] However, conventional MD was used for these studies, which may not be efficient enough to provide good sampling and therefore can lead to artificially overstabilized conformations. Furthermore, the conventional MD was also used to investigate the aggregation processes of Aβ monomers.[50−52] The structure of truncated Aβ oligomers have been simulated using replica exchange MDs (REMD).[53,54]

Motivated by results about toxicity of $A\beta_{1-42}$ oligomers and the importance of their structures in the self-assembly process,[24,25] in this work, we performed coarse-grained REMD and all-atom MD simulations for the $A\beta_{1-42}$ tetramer, one of the most toxic oligomers.[24] Because the system possesses large conformational varieties due to the presence of four flexible chains, we used the coarse-grained united residue (UNRES)[55−58] force field to reduce the computational cost and improve the sampling. The UNRES model allows one to simulate protein systems with an effective timescale of simulation of 3−4 orders of magnitude larger than all-atom methods. By using this model, we can simulate the tetramer at a significantly longer timescale and a wider temperature range than all-atom models but not requiring massive parallel computations. In the second step, classical all-atom MD simulations were used to assess the stability and refine the reconstructed coarse-grained models. Our results show that the Aβ tetramer is dominated by coil structures in an oblate spheroid shape. The different energies of the tetramer and fibril suggest a radical change in the structure of the oligomer to form the fibril, which is strictly connected to changing the three-dimensional structure of the small oligomer to the quasi-one-dimensional fibril. The solute−solvent interaction is responsible for the difference between oligomer and fibril structures.

The question of existence of water inside Aβ fibrils is under debate. Early experiments did not observe water molecules buried in the fibril core,[59] but more recent solid-state NMR experiments have provided evidence for their presence.[60,61] This result was also confirmed by all-atom MD simulation[62] using fibril structures which were resolved by the experiment and designed by the computer. The question of the difference between the distributions of water molecules in Aβ oligomers and fibrils remains open. In addition, because the water leakage may play a decisive role in neurotoxicity and oligomers are presumably more toxic than mature fibrils, we will consider this problem for the tetramer case.

The structures of $A\beta_{1-42}$ obtained in this work can also be used as initial conformations to build higher oligomers and in further studies of the amyloid aggregation process. Because in this study, the full-length structure of $A\beta_{1-42}$ was used, it will be called Aβ42 throughout the manuscript, instead of $A\beta_{1-42}$, for clarity.

2. MATERIALS AND METHODS

2.1. Generation of Initial Structures. To enhance the sampling of configuration space, we used various structures as the initial conformations for the UNRES REMD simulation. They were obtained using ClusPro 2.0 webserver (https://cluspro.bu.edu/), which is designed for protein−protein docking with high reliable results,[63] with the default scoring function used for docking simulations.[64] In the first step, 24 trimeric structures were obtained from the docking simulations using nine monomers taken from the study of Yang and Teplow,[36] and the dimer was taken from the study of Zhang et al.[40] In the second step, 24 trimeric structures obtained from docking and nine monomeric structures from the study of Yang and Teplow[36] were used to generate Aβ42 tetramers, from which 24 lowest energy structures of tetramers out of 216 generated and were used as initial structures in REMD simulation (Figure S1 in the Supporting Information) with 24 replicas.

Root-mean-square deviation (rmsd) of the docked structures was in the range from 9 to 24 Å from model 1 providing satisfactory diversity of initial models. The rmsd of the initial structures shows that these conformations are distinct and that they are located in very different points of the phase space. The initial tetrameric structures are dominated by statistical coil (Table 1), indicating that these structures are in unordered conformations. The helix propensity is rich and higher than the beta content (Table 1).

2.2. UNRES Coarse-Grained Model. In the UNRES model, the polypeptide chain is represented by a sequence of α-carbons (Cα's) linked by virtual bonds with attached united

DOI: 10.1021/acs.jpcb.9b04208
J. Phys. Chem. B XXXX, XXX, XXX−XXX

Table 1. Secondary Structure Content (%) of the Initial Structures Used for the REMD Simulation and the Structures from Two Periods of the REMD Run: 200−800 and 200−2000 ns at 296 K

structure	initial	200−800 ns	200−2000 ns
β	10.6 ± 2.1	19.5 ± 1.4	18.5 ± 2.7
α	20.0 ± 2.8	3.6 ± 1.1	2.7 ± 1.1
coil + turn	69.4 ± 6.5	76.9 ± 4.5	78.8 ± 7.1

side chains (SCs) and united peptide groups (p's) located in the middle between the consecutive α-carbons.[65] The united peptide groups and united side chains serve as interaction sites, while α-carbons assist the definition of geometry.[55] UNRES is a physics-based force field, in which most of the potentials of mean force were obtained not by statistical analysis of the pdb database but by ab initio and semiempirical calculations.[66] The newest version of the UNRES force field, optimized for protein structure folding[67] with periodic boundary conditions,[68] included in the UNRES package (http://unres.pl), was used to perform REMD simulation. Because the UNRES force field does not require any structural restraints in simulations, it can be used to study large conformational changes, such as protein folding and assembly of protein complexes.[69] The UNRES force field was found to be able to predict structures of the small and average-size proteins with good quality[70] and accurate enough to predict correctly structures and melting temperatures of the fibril-like protein with single amino-acid residue substitutions,[71] while older versions of the UNRES force field were successfully used to study the Aβ aggregation process.[72,73]

2.3. Replica Exchange Method. In this paper, 24 replicas with temperatures from 292 to 462 K were used. Each trajectory consisted 409 000 000 steps, each of 0.1 molecular time unit[56] (4.89 fs, which is a natural time unit if energy is expressed in kcal/mol, mass in g/mol, and distance in Å), providing 2000 ns. Replica exchanges were attempted every 1000 steps, and snapshots and other information were saved every 1000 steps. The dimensions of the cubic periodic box were set to 20 × 20 × 20 nm, which allows four Aβ42 chains to dissociate and associate during simulations to limit the bias coming from the initial structure but do not slow down the simulation due to the long binding time, resulting in Aβ42 concentration of 830 μM, which is higher than in the brain.[74] Simplification of the protein representation in coarse-grained models is the reason of smoothing the free energy landscape what leads to a much faster rate of observed phenomena comparing to all-atom methods.[75] Therefore, 1 ns of UNRES time corresponds to approximately 1−10 μs of real time.[56] However, for clarity, UNRES time is used in the rest of the manuscript. Twenty four tetramer structures obtained from docking were used for initial conformations (Figure S1) in REMD runs. The structures were sorted from the lowest docking energy to the highest which corresponded to the lowest and the highest temperature replicas.

2.4. Weighted Histogram Analysis Method. The weighted histogram analysis method (WHAM)[76] method, implemented in the UNRES package, was used to obtain structures of the Aβ42 tetramer at distinct temperatures[77] from the last 1800 ns of the REMD simulation. Subsequently, the tetramer structure ensemble corresponding to 295 K was clustered using Ward's minimum variance method[78] with rmsd cutoff between clusters set to 10 Å, to get representative structures, which were used as initial conformations for all-atom simulations (Figure 1).

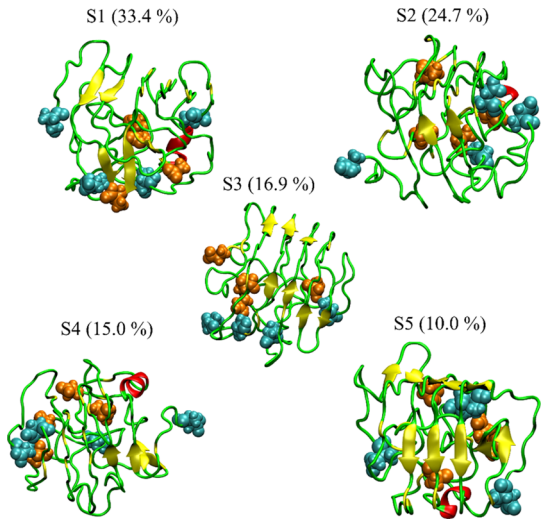

Figure 1. Cartoon representations of the reconstructed representative structures for five clusters obtained from UNRES REMD simulation. Cyan balls represent the N-termini, and orange balls represent the C-termini.

2.5. All-Atom MD Simulation. To investigate the stability of representative Aβ42 tetramer conformations, obtained in the coarse-grained REMD simulation, we analyzed these structures in all-atom force fields with the explicit solvent model. The MD simulations were carried out by the GROMACS 2016 package.[79] The leaf-frog algorithm was used to integrate the equations of motion with a time step of 2 fs. A cutoff of 1.0 nm was applied to electrostatic and van der Waals (vdW) forces, and the particle mesh Ewald method was used to calculate the long-range electrostatic interactions.[80] The covalent bonds were constrained by the LINCS algorithm.[81] Because the structures obtained from REMD simulation are coarse-grained conformations, pulchra software was used to reconstruct all-atom conformations from UNRES model structures.[82] Subsequently, the scwrl4 program was used to optimize side chains in the obtained all-atom models.[83] Then, MD simulations were run for these optimized structures with two setups: the tetramer is parameterized by AMBER99SB-ILDN[84] and OPLS-AA/L[85] force fields and then solvated in a cubic box by TIP3P[86] and TIP4P[86] water models, respectively. The simulation study suggests that these force fields provide the agreement between the secondary structure of the Aβ42 dimer and CD data.[87] The OPLS-AA/L force field produced results for monomer Aβ40 that agree with experimental data.[88] Furthermore, AMBER99SB-ILDN shows that this force field can successfully reproduce NMR results of Aβ40.[89,90] To neutralize the charge of the systems, 12 Na^+ counter ions were added. The systems were minimized by the steepest descent algorithm and equilibrated for 500 ps in the NVT ensemble at 300 K kept by the v-rescale algorithm[91] followed by 10 ns in the *NPT* ensemble at 300 K and 1 bar. Finally, the production MD simulations were performed for 200 ns at constant temperature and pressure conditions. For each representative structure from REMD, five independent MD trajectories were conducted.

The equilibrium procedure for four chains extracted from the Aβ42 fibril structure (PDB code 2NAO[27]) was the same as

DOI: 10.1021/acs.jpcb.9b04208
J. Phys. Chem. B XXXX, XXX, XXX−XXX

for our tetrameric models. Then, five independent trajectories of production MD simulations were carried out for 20 ns with restraints placed on Cα atoms with a spring constant of 1000 kJ/mol/nm to preserve the fibril structure and allow water molecules to equilibrate and properly solvate the system. Simulations were run at the constant temperature and pressure conditions, and snapshots from last 10 ns were used for data analysis.

2.6. Tools for Data Analysis. *2.6.1. rmsd and RMSF.* Structural changes and dynamics of the Aβ42 tetramer were studied using the rmsd and root-mean-square fluctuations (RMSF). The initial conformations from MD runs were used as references to calculate both rmsd and RMSF. The fluctuation of the atom j is given by the following equation

$$\mathrm{RMSF}_j = \sqrt{\frac{1}{n}\sum_{i=1}^{n}(r_{i,j} - r_{0,j})^2} \quad (1)$$

where n is the number of analyzed snapshots, $r_{i,j}$ is the position of atom j in snapshot i, and $r_{0,j}$ is the position of atom j in the initial structure.

2.6.2. Secondary Structures. The STRIDE algorithm[92] was used to calculate the propensity of secondary structures of the tetramer. Based on both dihedral angles and hydrogen bond, it is less sensitive to imperfections resulting from conversion of coarse-grained models to all-atom structures.

2.6.3. Interchain Contacts and Oligomer Size. Interchain contacts were examined by calculating the distance between side chain centers of mass of two residues from different monomers, and the contact was detected if it was less than 6.5 Å. To determine the size of the oligomer, we used the criterion that two chains are considered as part of an oligomer if they have at least five interchain contacts, which allows to exclude contribution of the weak interactions between chains due to their accidental proximity during simulations. The structures from coarse-grained REMD simulation are used to assess number of interchain contacts.

2.6.4. Hydropathy. We used the hydropathy indexes from the study of Kyte and Doolittle.[93] The total hydropathy is the total value of hydropathy of residues which form contacts. In this work, if one residue forms multiple contacts, its hydropathy contribution is proportional to the number of contacts.

2.6.5. Residues Binding New Chains to Dimer and Trimer to Form Tetramer. When the tetramer is formed from smaller oligomers as two interacting dimers or trimer interacting with the monomer, the residues of different oligomers forming interchain contacts are calculated. Then, the population of contacts is obtained from the ratio between the number of contacts of these residues and the number of tetramer formations from different structures.

2.6.6. Radial Distribution. The distances between the charged atoms and the center of mass of the oligomer are calculated and histogrammed.

2.6.7. Water Molecules Located inside the Oligomer. To calculate the number of water molecules in the oligomer, the quickhull algorithm was utilized to construct the convex hull of the oligomer.[94] Then, the concave hull of the oligomer was generated using the algorithm proposed by Park and Oh with a threshold of 5.[95] Finally, water molecules which are inside the concave hull are counted as internal water molecules.

2.6.8. Clustering. The gmx cluster tool from the GROMACS package was used to cluster structures of the tetramer from canonical MD simulations, using the GROMACS algorithm[96] with a cutoff of 2.5 Å.

2.6.9. Eccentricity. The protein was fitted in the ellipsoid centered at the center of mass with semiaxes a, b, and c. When $c < a$, the ellipsoid is called oblate spheroid and prolate spheroid when $c > a$. The eccentricity is calculated as $e = \sqrt{1 - \frac{c^2}{a^2}}$ when $c < a$ and $e = \sqrt{1 - \frac{a^2}{c^2}}$ when $c > a$. The semiaxes are calculated from moments of inertia I_1, I_2, and I_3 using the following equations

$$I_1 = \frac{2}{5}m(b^2 + c^2),\ I_2 = \frac{2}{5}m(c^2 + a^2),\ \text{and}\ I_3 = \frac{2}{5}m(a^2 + b^2)$$

Here, the mass of the tetramer is m = 18.024 kDa. The three moments of inertia are calculated by diagonalizing the inertial tensor using the gmx principal tool from the GROMACS package.

2.6.10. Height of Tetramer. Based on the moments of inertia I_1, I_2, and I_3, we calculated a, b, and c semiaxes from the equations: $a^2 = \frac{5}{4m}(I_2 + I_3 - I_1)$, $b^2 = \frac{5}{4m}(I_1 + I_3 - I_2)$, and $c^2 = \frac{5}{4m}(I_1 + I_2 - I_3)$. The height of the tetramer is the smallest half-axis multiplied by 2.

2.6.11. Transition Network. Based on the idea of the transition network from previous studies,[51,52,97,98] we constructed the transition network as follows. The state of the oligomer in all-atom simulations was defined as a combination of two numbers: shape index of the oligomer (ratio between the lowest and the highest moment of inertia, I_{min}/I_{max}, multiplied by 10 and rounded to the nearest integer) and the number of interchain contacts, while in the REMD coarse-grained simulation, the oligomer size was used as an additional property. For all-atom simulations, the transition matrix was calculated from all equilibrated parts of the MD trajectories, whereas for the coarse-grained simulation, whole 24 trajectories were used. First, N states of the oligomer were determined in the simulations. Then, the $N \times N$ matrix was constructed, in which the value at i row and j column is the population of transition from state i to j. The data in the rows of the transition matrix were normalized. On the transition graph, the color of the nodes represents the state index, and the color of the edges represents the transition between two states with a nonzero population. The node area and the edge thickness correspond to the population of the state and the transition probability between two states, respectively. The Gephi visualization and exploration software were used to visualize the transition network, and the node distribution was optimized using the Force Atlas algorithm.[99]

2.6.12. Collision Cross Section. Ion mobility of the Aβ42 systems was estimated by theoretical calculations of collision cross-section (CCS) values using the trajectory method (TM) implemented in the Mobcal software[100,101] for representative structures of dominant clusters from all-atom MD simulations. In the TM model, instead of using hard core radius, other effects such as ion-induced interactions are included. While theoretical CCS values are difficult to interpret independently, they are very useful for the comparison with the experimental observations.[102]

2.6.13. Hydrophobic Solvent Accessible Surface Area. The tool gmx sasa from the GROMACS package was used to

DOI: 10.1021/acs.jpcb.9b04208
J. Phys. Chem. B XXXX, XXX, XXX−XXX

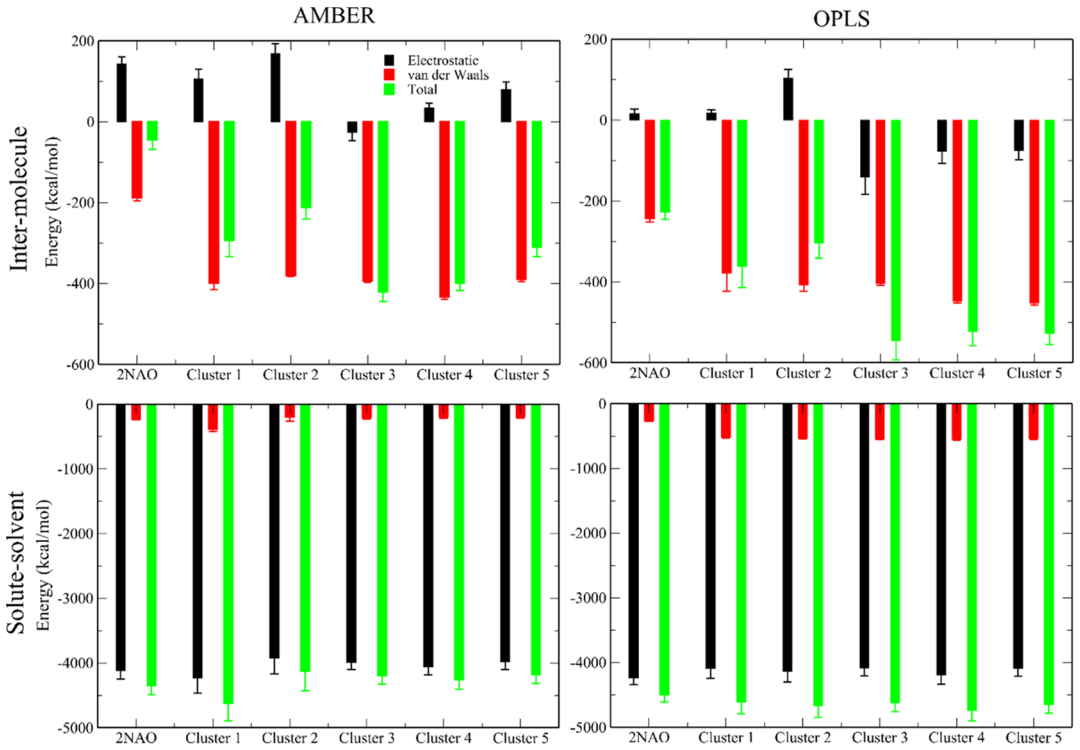

Figure 2. Electrostatic and vdW energy components (kcal/mol) for intermolecular (intermolecular interaction energies between chains of tetrameric structures) and solute−solvent interactions (intermolecular interaction energies between tetrameric structures and water and ions). For 2NAO, the result was averaged over snapshots for the last 10−20 ns period of MD simulations, whereas for five representative structures for each of the five trajectories (25 structures in total). Error bars represent standard deviations.

calculate hydrophobic solvent accessible surface area (hSASA).[103] In this work, residues treated as hydrophobic are as follows: glycine (Gly), alanine (Ala), valine (Val), leucine (Leu), isoleucine (Ile), proline (Pro), phenylalanine (Phe), methionine (Met), and tryptophan (Trp).

2.6.14. Dipole Moment. Dipole moment of the system $\vec{\mu}$ is defined as follows

$$\vec{\mu} = \sum_{i=1}^{N} q_i \vec{r_i}$$

where q_i and $\vec{r}_i$ are charge and position vectors of atom i, and N is the total number of atoms.

3. RESULTS AND DISCUSSION

3.1. Convergence of Coarse-Grained Simulations. Coarse-grained simulation was performed using the REMD method starting from 20 different orientations of chains to enhance sampling. The acceptance ratio between replicas was above 31% between any pair of neighboring replicas providing good exchanges between temperatures. This is also evident from the random work in the replica space (Figure S2), showing that the exchange occurred between any pair of neighbored replicas.

Cα-rmsd at 296 K (Figure S3) shows that the system is stable from approximately 200 ns, so the first 200 ns was discarded in further analysis. However, based on rmsd, we cannot be sure of achieving equilibrium because in REMD simulations, chains can switch places and conformations in the oligomer,[42,104] making the rmsd definition ambiguous. Therefore, to examine if the simulation converged, the trajectory at 296 K was split into two time windows, 200−1100 and 200−2000 ns, which were subsequently used for WHAM and clustering analysis. The heat capacity (C_v) obtained from the WHAM analysis (Figure S4) is virtually identical for these two time windows, which means that we have at least reached quasi-equilibrium. In addition, the secondary structures of reconstructed all-atom representative structures from both time windows are similar (Table 1), providing additional support for this conclusion. Therefore, only the 200−2000 ns time window was used in further analysis.

Note that the heat capacity has a peak at T = 297 K (Figure S4), which indicates the dissociation temperature of the tetramer. A similar result was obtained for the dimer of the acshorter Aβ peptide.[105]

3.2. Tetramer Structure from REMD Simulation. At 295.6 K, the converged part of the simulation was used for clustering to obtain five groups of structures, from which cluster centroids were selected as representative models (Figure 1). Clustering criteria provided low diversity within clusters (rmsd below 1.5 Å) with large diversities between clusters (rmsd in range 6.2−12.0 Å). These models will be used in all-atom simulation. Clusters 1, 2, 3, 4, and 5 constitute 33.4, 24.7, 16.9, 15.0, and 10.0% of all structures, respectively. The low propensity of beta strands in tetrameric structures from REMD simulations (Table 1) shows that they are still in a disordered state. The short beta strand in monomers form the parallel beta sheet (Figure 1), but this structure is still different from fibril structures of Aβ,[26,27] in which monomers form a "cross-beta" structure. There are multiple suggested structures of Aβ oligomers (e.g., barrel-like); however, most of them are constructed using truncated parts of Aβ,[106−108] and there is no experimental evidence that such conformations can be present in nature for a full sequence of Aβ42. The all-atom

DOI: 10.1021/acs.jpcb.9b04208
J. Phys. Chem. B XXXX, XXX, XXX−XXX

Table 2. Secondary Structure Content (%) Averaged over the Snapshots Collected from 100−200 ns Period of all MD Simulations for five Representative Structures[a]

structure	force field	cluster 1	cluster 2	cluster 3	cluster 4	cluster 5	2NAO
beta	AMBER	16.8 ± 1.9	18.2 ± 1.8	21.1 ± 1.9	19.3 ± 2.2	21.9 ± 2.1	40.0 ± 1.1
	OPLS	21.9 ± 2.4	21.0 ± 2.1	19.8 ± 1.9	12.7 ± 1.7	20.3 ± 2.2	34.7 ± 0.8
helix	AMBER	4.7 ± 0.7	2.4 ± 0.5	1.0 ± 0.2	1.1 ± 0.3	2.0 ± 0.3	0.0 ± 0.0
	OPLS	3.2 ± 0.9	2.0 ± 0.6	0.5 ± 0.1	1.1 ± 0.3	0.2 ± 0.0	0.0 ± 0.0
turn	AMBER	35.9 ± 2.1	41.4 ± 2.1	37.1 ± 1.9	36.8 ± 2.2	40.2 ± 2.2	26.7 ± 0.8
	OPLS	41.5 ± 2.4	39.3 ± 2.3	43.2 ± 2.0	40.0 ± 2.4	38.4 ± 2.2	30.0 ± 1.7
coil	AMBER	42.6 ± 2.2	38.0 ± 1.9	40.8 ± 1.9	42.8 ± 2.1	35.9 ± 2.1	33.3 ± 1.0
	OPLS	33.4 ± 2.3	37.7 ± 2.1	36.5 ± 2.0	46.2 ± 2.2	41.1 ± 2.4	35.3 ± 1.0

[a]For 2NAO, the results were obtained using snapshots collected for 10−20 ns period of MD simulation. Error bars represent standard deviations.

structures of the five clusters in the PDB file format are attached in the Supporting Information.

3.3. Distribution of Interchain Contacts and Oligomers in UNRES. We calculated the number of side chain contacts between chains in the oligomer. The histograms of interchain contacts (Figure S5) show that the interactions between different pairs differ significantly from each other. The population of interchain contacts between chains A and B is the smallest, and at temperatures around 300 K, the average number of contacts is 5. Therefore, in this work, we used five contacts as the criterion to determine whether two chains are in the same oligomer or not. Using this criterion we obtained the distribution of oligomer size showing that at high temperatures, the tetramer decomposes into monomers, dimersm and trimers due to the significant populations of these molecules at high-temperature replicas (results not shown). At lower temperatures, the monomers cannot decompose leading to the stable structure of the tetramer. This result shows that the Aβ42 tetrameric structures are formed by two processes: addition of the monomer to the seeds at high temperature and the structural rearrangement at low temperature replicas. These processes eliminate any bias coming from the initial structures from docking as well as speed up the tetramer formation because the distance between the monomers is small enough.

3.4. All-Atom Simulations. In the next step, conventional all-atom MD simulations were performed at 300 K with AMBER99SB-ILDN and OPLS-AA/L force fields using reconstructed coarse-grained models (Figure 1) as the initial conformations. All MD trajectories are stable from about 100 ns (Figure S6), so snapshots from 100−200 ns range were used for clustering and further analysis.

To compare the obtained tetrameric structures with the more organized fibril-like structure, four chains from the Aβ42 fibril (PDB code: 2NAO[27]) were extracted and used to perform five MD trajectories of 20 ns in two all-atom force fields. Because Cα atoms were restrained, rmsd with respect to the 2NAO structure is small (about 0.47−0.61 Å).

3.5. Representative Structures in All-Atom Simulations. Similar to coarse-grained simulations, five representative structures were obtained, which are cluster centroids of the largest clusters from all trajectories starting from coarse-grained models (Figures S7). In total, we have 50 representative structures for Amber and OPLS force fields. By clustering the snapshots obtained in the last 10 ns of the simulation which started with the 2NAO PDB structure, we obtained the two most populated structures for these force fields (Figure S7).

3.6. Analysis of the Energy Components. The intermolecular interaction energy was calculated for the representative structures of the first clusters from MD trajectories (Figure S7) starting from coarse-grained models and compared to the analogous simulations starting from the tetrameric structure from the 2NAO pdb file (Figure S7). In the case of 2NAO, the impact of the force field on the energy is strong (Figure 2). The electrostatic component is positive in both force fields AMBER99SB-ILDN and OPLS-AA/L, and their values in these force fields are substantially different. In the AMBER force field, UNRES cluster 2 has a slightly higher electrostatic energy compared to 2NAO leading to the fact that its total interaction energy exceeds other clusters (Figure 2). All clusters, in particular cluster 3, have less energy than 2NAO. Therefore, in terms of the solute energy, representative compact structures, obtained by UNRES and all-atom simulations, are more favorable than fibril-like structure 2NAO.

In the OPLS-AA/L force field, cluster 1 has equivalent energy with 2NAO within the error range. Similar to the AMBER force field, cluster 2 has higher electrostatic energy than 2NAO, while others have lower energy than 2NAO (Figure 2).

In the case of electrostatic energy, the difference between the clusters is significant in both force fields (Figure 2). The electrostatic energy of 2NAO and our tetramer structures in the OPLS-AA/L force field is lower than in AMBER99SB-ILDN. The difference in electrostatic energy between the clusters indicates that the structures of the tetramer are polymorphic because electrostatic energy is sensitive to conformation. In terms of vdW energy, the difference between the UNRES clusters is insignificant. Except cluster 1, this energy component in OPLS-AA/L is lower than in AMBER99SB-ILDN, suggesting a denser tetramer package than in the AMBER99SB-ILDN force field. This situation is similar to the case of 2NAO, where the vdW energy in OPLS-AA/L is lower than in AMBER99SB-ILDN.

In all our tetrameric structures and structures of 2NAO, the vdW component prevails in the nonbonded energy, and it is significantly larger than the electrostatic component (Figure 2). Furthermore, the difference between the nonbonded molecular interaction energies of 2NAO and our tetrameric structures is very sensitive to the structure indicating that the potential barrier for conversion of our tetramer to fibril is significantly diverse. This result suggests the existence of multiple oligomerization pathways and that the tetramer can easily form fibrils or must rearrange the conformation or favor the oligomer state due to the strong nonbonded interaction energy.

DOI: 10.1021/acs.jpcb.9b04208
J. Phys. Chem. B XXXX, XXX, XXX−XXX

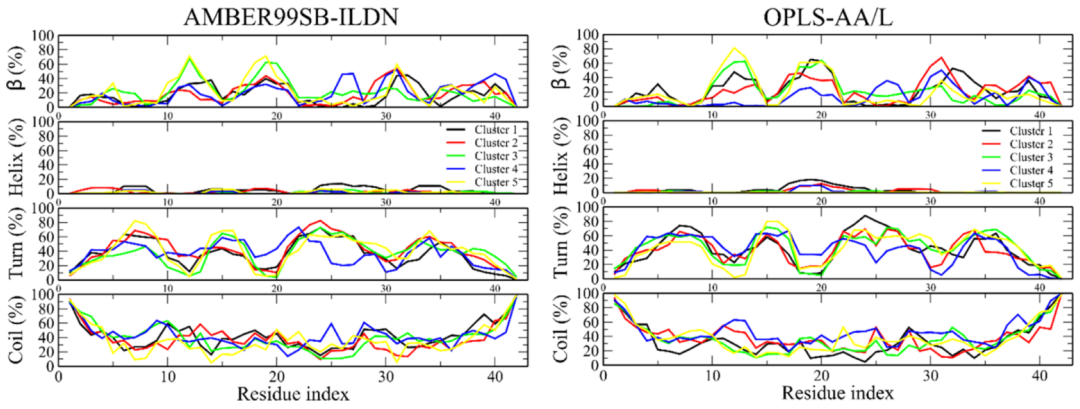

Figure 3. Distribution of average secondary structures calculated using all snapshots from 100−200 ns period of all-atom MD simulations.

On the other hand, the tetrameric Aβ42 interaction with a solvent is approximately an order of magnitude higher than the internal energy of the tetramer (Figure 2). These interactions are dominated by the electrostatic component, which suggests that oligomers tend to form a hydrophobic core. In OPLS, the nonbonded interaction energy between our models and the solvent is lower than that of 2NAO solvent, implying that the extended fibril structure is less favorable.

3.7. Secondary Structures of Representative Structures. The secondary structure content of representative structures of the five clusters from all-atom simulation (Table 2) shows that in both force fields, tetrameric Aβ42 is dominated by turn and coil, indicating the disordered state, which is consistent with experimental observations.[3] The percentage of beta structures in both force fields is equivalent to REMD simulation (Table 1). However, the beta propensity of REMD cluster 1 in the OPLS-AA/L force field is higher than AMBER99SB-ILDN, but cluster 4 has lower beta in OPLS-AA/L. The beta population of other clusters in both force fields is equivalent (Table 2). With the exception of cluster 1, in MD simulations, the helix structure is lower than in REMD, and in both cases, the propensities are low (Tables 1 and 2). For 2NAO, the beta content is about 40 and 35% in Amber and OPLS, respectively (Table 2), and these values, as expected, are higher than those of the five REMD clusters. The helix structure did not occur in 2NAO, while the turn is lower than the coil, but they vary between 27 and 33% depending on the force fields.

The distribution of secondary structures of the Aβ42 tetramer (Figure 3) is similar in both force fields. The beta structure concentrates in residues 9−14, 17−21, and 30−40 are in agreement with experimental data on the Aβ40 oligomer (regions 7−12, 17−26, and 30−39).[109] The region of 11−21 residues has the highest beta propensity (Figure 3) which is consistent with simulation results of Brown and Bevan (residues 17−21).[49] The C-terminus has a lower beta propensity than these residues, and it is slightly higher in OPLS-AA/L than in the AMBER99SB-ILDN force field (17.7 and 14.2%, respectively). The concentration of the beta structure in the residues 11−21 and the C-terminus is also in agreement with previously theoretical studies of the Aβ42 monomer[39,110,111] and experimental data of the Aβ42 fibril.[27,28] However, the average level of beta is lower than that of oligomers (44%),[112] but this result is reasonable because oligomers studied by studied by Ahmed et al.,[112] have more chains than tetramers. On the other hand, the obtained beta content is lower than in monomers.[113] The short α-helix structure is rarely observed in the N-terminus and 20−30 residue range, with insignificant population.

The secondary structures, obtained for each chain in MD simulations, show the difference between two force fields (Table S1). In AMBER99SB-ILDN, four chains have equivalent beta propensity in clusters 3 and 4 within the error range. The distribution of secondary structures for each chain (Figure S8) is distinct from others, especially turn and coil structures. In OPLS-AA, the chains have various average beta populations, and other secondary structure propensities of residues are also different (data not shown), similar to the AMBER99SB-ILDN force field. These results indicate a distinct character of the chains in the oligomeric tetramer as it differs from fibril structures, in which properties of chains are homogenous. The difference may be due to the different exposition of the chains to the solvent in the tetrameric structures.

3.8. Chains Display Different Flexibilities. In coarse-grained simulations, the RMSF of the chains in the tetramer (Figure S9) shows that in chains 2, 3, and 4, the N-terminus and region 20−30 are more flexible than 10−20 and 30−40 regions. In the case of chain 1, the N- and C-terminal residues are more flexible than others. In all-atom simulations (Figure S10), regions 20−30 and C-terminus are more flexible than other domains. In case of chain 2 and 3, regions 10−20 and C-terminus are more flexible than other regions in the AMBER99SB-ILDN force field (Figure S10). However, in OPLS, the difference is not that pronounced as in the AMBER99SB-ILDN force field. The region close to the C-terminus is significantly more flexible in OPLS (Figure S10). These results show the different impact of force fields on dynamics of the amino-acid residues.

3.9. Shape of Aβ42 Tetramer. To determine the compactness of the Aβ42 tetrameric structure, we calculated R_I—the ratio of the smallest component of the moment of inertia and the largest one for the structures in the equilibrated part of MD trajectories. This quantity is similar to parameter N4 used by Barz et al[52] For direct comparison with results of Barz et al.[52] R_I is multiplied by 10 and rounded to the nearest integer. The tetramer conformation is called "compact" when R_I is larger than 5 and "extended" with the ratio less or equal to 5. The population of "compact" and "extended" conformations of the Aβ42 tetramer from two force fields is similar. In both force fields, the tetramer favors the "compact" structure; however, OPLS-AA/L preserves "compact" conformation stronger than AMBER99SB-ILDN.

DOI: 10.1021/acs.jpcb.9b04208
J. Phys. Chem. B XXXX, XXX, XXX−XXX

In the study of Barz et al.,[52] the Aβ42 tetramer structures exist in extended conformation or compact conformation which have a prolate or oblate spheroid shape, respectively. For more detailed information on the shape of the Aβ42 tetramer, the eccentricity of structures obtained from MD simulation was calculated. The semiaxes show that the structures are in the oblate spheroid state ($c < a$); the eccentricity values (Table 3) indicate that the tetramer structures are in the disc-like state, which is consistent with Aβ42 oligomers described by the experiment of Ahmed et al.[112] Brown and Bevan[49] also obtained an oblate spheroid in all-atom simulations, in which ratio R_I is 6, and the eccentricity is 0.79 ± 0.03. The oblate spheroid state of the Aβ42 tetramer in this work is also consistent with the Aβ_{18-41} tetramer structure from Streltsov et al.[114] in which the eccentricity value is ~0.8 ($c < a$). However, using mass spectrometry, being an in vacuo technique, Bernstein and coworkers[115] found that the Aβ42 tetramer comprises two dimer subunits making an angle of 120° a planar plane. The effect of the solvent may be responsible for the difference between our results and Bernstein et al.[115]

Table 3. Eccentricity of Aβ42 Calculated Using the Snapshots from 100−200 ns Period of all MD Simulations[a]

REMD cluster	AMBER99SB-ILDN	OPLS-AA/L
1	0.67 ± 0.07	0.59 ± 0.05
2	0.75 ± 0.09	0.68 ± 0.05
3	0.82 ± 0.05	0.71 ± 0.07
4	0.73 ± 0.06	0.67 ± 0.07
5	0.71 ± 0.08	0.67 ± 0.05
2NAO	0.98 ± 0.01	0.98 ± 0.01

[a]For 2NAO, we used the snapshots from the 10−20 ns period of simulation.

We have calculated the height of oligomers and 2NAO using the definition given in Materials and Methods and snapshots collected from the 100−200 and 10−20 ns period of all-atom MD simulations for five clusters and 2NAO, respectively. The height of the tetramer models was in the range of 2.0−2.2 nm, in contrast to the 0.98−1.0 for four chains of 2NAO. Our result is in agreement with Ahmed et al.[112] who reported that the height of oligomers of different sizes varies from ≈2 to 5 nm.

3.10. Collison Cross Section of Tetrameric Aβ42. The results of CCSs of the Aβ42 tetramer (Table 4) show that all REMD clusters have similar cross-section values within error ranges, except cluster 3. The difference between two all-atom force fields is small, indicating that the shape of the tetramer in both force fields is the same that is consistent with eccentricity results. In general, the structures in AMBER99SB-ILDN are slightly less compact; therefore, their eccentricity and CCSs are slightly higher than in the OPLS force field. Our values (Table 4) are lower than experimental data of Bernstein et al.[115] which is 2332 Å^2. However, the CCSs are consistent with the result from Zheng et al.[116] Using the TM, Barz and coworkers obtained 2109 ± 3 and 1978 ± 9 Å^2 for CCS of Aβ42 from MD simulation with implicit solvent which is not far from our results.[52] This result also indicates that the Aβ42 tetramer is in disc-like conformation because the CCS values are equivalent to packed model in Bernstein et al., which is 2135 Å^2.[115] Overall, in terms of CCS, cluster 3 agrees with the experiment[115] better than other models. The CCS value for 2NAO is significantly higher than any experimental and computational values, confirming our conclusion that the fibril is less compact than oligomers. However, it should be noted that CCSs values are just rough estimated, subjected to uncertainty of the prediction tool, and they do not take into account the ionization and gas phase, respectively, for theoretical and experimental methods.

Table 4. CCSs for Aβ42 Tetramer Clusters Calculated Using Snapshots Collected from the 100−200 ns Period of All-Atom MD Simulations[a]

		collision cross section (Å^2)	
		AMBER99SB-ILDN	OPLS-AA/L
UNRES cluster	1	2029.6 ± 48.6	1946.6 ± 27.4
	2	2084.7 ± 60.4	2009.2 ± 46.7
	3	2159.1 ± 86.2	1988.8 ± 37.9
	4	2034.2 ± 44.8	1997.8 ± 35.7
	5	2038.2 ± 62.7	2002.1 ± 42.4
2NAO		2649.1 ± 46.4	2656.4 ± 36.0

[a]Result for 2NAO was obtained using snapshots from the 10−20 ns period.

3.11. Hydrophobic Solvent Accessible Surface Area. The solvent accessible surface area for hydrophobic residues was calculated for the equilibrated part of the MD trajectories (Figure 4). The average hSASA values in the OPLS-AA/L force field are smaller than in AMBER99SB-ILDN (Table 5), which is consistent with the result of compact conformation population in force fields. The areas in the OPLS-AA/L force field are also smaller than results from Barz et al.[52] (4833 and 5027 Å^2) and Brown and Bevan[49] (~5400 Å^2). In the case of the AMBER99SB-ILDN force field, clusters 2 and 3 have consistent values with the compact structure (4833 Å^2) and extended structure (5027 Å^2) from Barz et al.,[52] respectively. As shown above, our tetrameric structures favor a compact state.

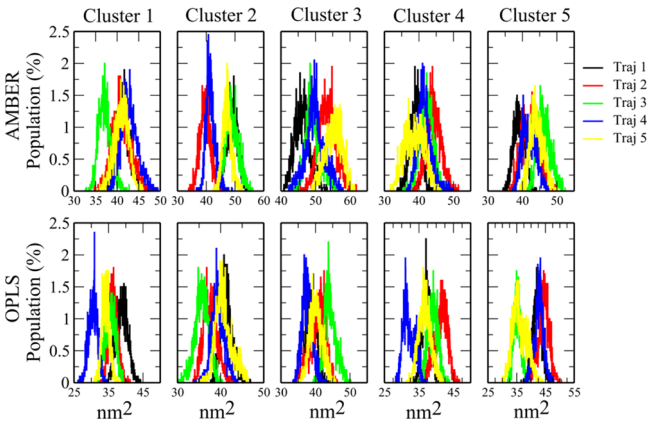

Figure 4. hSASA of the Aβ42 tetramer calculated using all snapshots from the 100−200 ns period of all-atom MD simulations.

Although our cluster 3 is compact, its hSASA is close to that of the extended structure reported earlier.[52] This can come from the solvent model, which is an implicit solvent in the previous study,[52] while we used an explicit solvent. This is also supported by the result obtained for hSASA of the compact structure with an explicit solvent,[49] which is close to the value of cluster 3. The hSASA values of other clusters in the AMBER99SB-ILDN force field are smaller than results from

DOI: 10.1021/acs.jpcb.9b04208
J. Phys. Chem. B XXXX, XXX, XXX−XXX

Table 5. hSASA of the Aβ42 Tetramer, Total Hydropathy Index[93] of the Residues That Have Interchain Contacts, and Number of Water Molecules in the Polyhedrons Built From Tetramer Structures[a]

	hSASA (Å^2)		total hydropathy		AMBER99SB-ILDN		OPLS-AA/L	
UNRES cluster	AMBER99SB-ILDN	OPLS-AA/L	AMBER99SB-ILDN	OPLS-AA/L	number of waters	molar concentration [M]	number of waters	molar concentration [M]
1	4074.9 ± 88.7	3516.5 ± 178.7	390.8 ± 20.2	420.3 ± 21.2	158 ± 40	2.7 ± 0.4	120 ± 34	2.2 ± 0.4
2	4530.7 ± 183.2	3899.5 ± 235.4	293.3 ± 19.2	331.2 ± 19.4	179 ± 63	2.7 ± 0.4	144 ± 34	2.3 ± 0.4
3	5117.3 ± 190.8	4039.6 ± 151.4	240.5 ± 19.6	300.9 ± 20.0	150 ± 48	2.2 ± 0.5	178 ± 44	2.7 ± 0.5
4	4117.1 ± 247.8	3731.3 ± 142.1	395.5 ± 22.3	432.8 ± 22.2	137 ± 37	2.3 ± 0.4	123 ± 33	2.15 ± 0.4
5	4280.8 ± 172.9	4013.9 ± 156.6	287.1 ± 19.4	329.2 ± 20.0	147 ± 42	2.5 ± 0.4	163 ± 40	2.7 ± 0.5
2NAO	5355.1 ± 34.9	5354.9 ± 30.6	192.3 ± 16.7	192.9 ± 17.1	65 ± 4	0.8 ± 0.1	68 ± 11	0.9 ± 0.1

[a]These results are calculated using all snapshots from 100−200 and 10−20 ns periods of all-atom MD simulation for our tetrameric models and four chains of 2NAO, respectively.

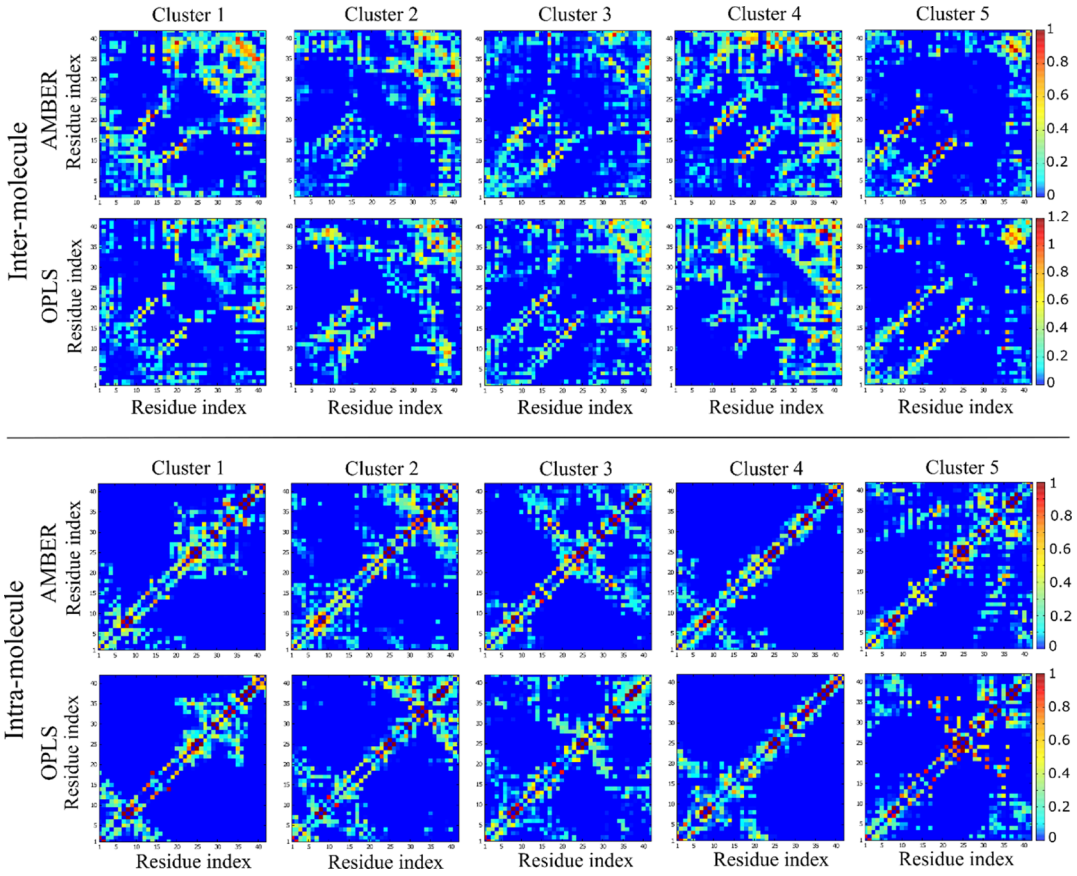

Figure 5. Intermolecular (upper part) and intramolecular (lower part) contact maps averaged over all snapshots from the 100−200 ns period of all-atom MD simulations.

previous studies[49,52] (Table 5). Therefore, the estimation of hSASA supports the observation that our tetrameric structures are in a compact state. The hSASA of four chains of 2NAO is larger than all clusters in the AMBER force field, except cluster 3 (Table 5). However, in OPLS-AA/L, all our tetrameric structures have lower hSASA than 2NAO (Table 5) because the 2NAO structure is more extended.

3.12. Contact Maps of Aβ42 Tetramer. The intermolecular contact maps for five MD trajectories of two clusters from REMD show a high propensity to form interactions in regions (30−42)−(30−42) in both force fields (Figure 5). This result indicates that the C-terminus plays an important role in stabilization of the Aβ42 tetramer. In addition, strong contacts in the C-terminal region of a small oligomer as a tetramer indicates the seeding role of this region in Aβ42 self-assembly, which is consistent with results from discrete MD of Urbanc et al.[117] Interchain contacts between residues (10−25)−(10−25) and (30−42)−(1−20) also have significant populations, which are in agreement with the results of Barz et al.[52] However, the population in our contact maps is higher, suggesting that the tetramer structures in our work are more rigid than Barz's conformations.

To explore the different behaviors of each chain in the tetramer, we separated the contact map for each of the chains (Figure S11). Chains B and D have the strongest contact, indicating that they are located in the tetramer core. The contacts of these chains are concentrated in areas (15−25)−(15−25) and (30−42)−(30−42). Because these chains are in

DOI: 10.1021/acs.jpcb.9b04208
J. Phys. Chem. B XXXX, XXX, XXX−XXX

the tetramer core, this result strengthens the conclusion that these regions play an important role in stabilizing the tetramer. Chain A and C have lowest number of contacts suggesting that they are in the outer shell of the tetramer (Figure S11). Although these chains form weak contacts, they are also concentrated in regions (15−25)−(15−25). Consequently, all tetramer chains have the same contact motif, but water molecules act on the outer shell chains leading to weaker contacts in these chains.

3.13. Transition Network. The population of the states determined by the oligomer size (Figure 6) from the coarse-grained REMD simulation shows that the tetrameric structure has the highest propensity (76%), implying that the system still retains tetramer conformation in the REMD simulation. The probability of a process 2 + 2 → 4 (83.8%) is higher than 3 + 1 → 4 (73.7%), which suggests that the tetramer is more likely to be formed from two dimers than from a trimer and monomer and from four monomers (50.6%). Furthermore, the population of dimers is larger than the trimers, and the probability of 4 → 2 + 2 is higher than the 4 → 3 + 1 process (Figure 6), confirming the observation that the tetramer is formed from the dimer−dimer association more often than from the trimer−monomer. This result is consistent with Barz et al.[52] who observed the critical role of the dimer in the formation of higher order oligomers. The probability of 3 + 1 → 2 + 2 is higher than 2 + 2 → 3 + 1 (Figure 6), which shows that the complex of the trimer and monomer is less stable than two dimers. The full transition network (Figure S12) also shows that the tetramer states are located closer to the two dimer state than the trimer−monomer state, which indicates that the transition between these states is easier and more frequent than the trimer−monomer to tetramer.

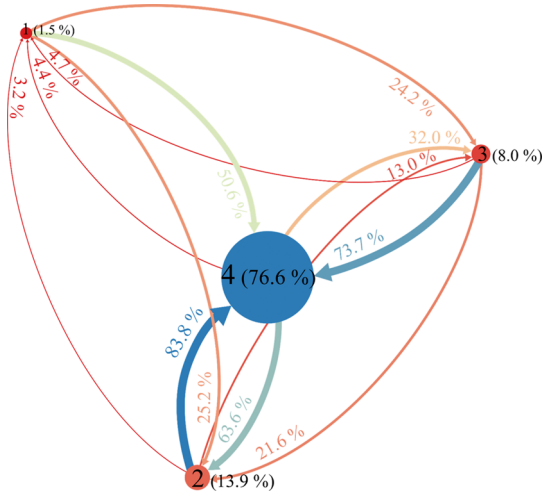

Figure 6. Coarse-grained transition network from UNRES REMD simulation averaged over all replicas. Oligomer size is shown as a label on each node, while the area of nodes corresponds to the population of each state, which is also shown in brackets. Colors of the lines with arrows and their labels represent exchange rates between nodes (different oligomer sizes).

Transition networks for the tetramer in all-atom simulations are divided into distinct regions (Figure S13), showing that the tetramer can exist in states with different shapes. Moreover, the large distance between states with a big difference in the shape index indicates that the free energy barrier between these states may be high. Consequently, the tetramer conformation is polymorphic, and this is due to the fact that the Aβ peptide is intrinsically disordered. States, separated by a large distance of shape index, are metastable because the transition between them is practically forbidden.

3.14. Most Probable Structure of Aβ42 Tetramer. Based on the above results, we now study the most probable structure from five clusters, obtained from UNRES REMD simulation. Experimental studies have shown that the Aβ42 oligomer has turns at residues 24−27,[118] 25−28,[119] 13−15, 25−29, and 37−38.[112] These turns connect β-strand at regions 13−23, 28−42,[118] 15−24, 29−42,[119] 17−21, and 31−36.[112] Furthermore, Streltsov et al. showed that the Aβ_{18-41} tetramer comprises turns at residues 24−26, β-elements in the region 18−21, and a β-hairpin at residues 32−41.[114] In our tetrameric structures, all clusters have high β-propensity at residues 10−15, 16−19, 30−34, and 38−40 (Figure 3). However, cluster 4 has a β-strand in residues 25−28 which is inconsistent with experiments, while other clusters have a rich turn propensity in regions 5−9, 13−15, 23−27, and 34−38. This result indicates that secondary structure elements of clusters 1, 2, 3, and 5 are consistent with experimental data.

As shown above, the CCS values of all clusters are lower than the experimental value of Bernstein[115] but consistent with Zheng et al.[116] (2172 Å^2). Cluster 3 (2159.1 ± 86.2 Å^2) is best consistent with the result of Zheng et al. in the AMBER99SB-ILDN force field. In the case of hSASA results, clusters 2 and 3 have consistent results with other studies. Ahmed et al. have shown that residue Phe19 has intramolecular contact with Leu34,[112] and the region 17−21 has an interaction with 31−36. The results for intramolecular contacts of all clusters (Figure 5) indicate that clusters 3 and 5 form contacts between residues 15−20 and 30−35, while others have a weak contact propensity in this region. We can show that the population of the Phe19−Leu34 intramonomer contact is ≈36% for cluster 3 in OPLS, while it is very poorly populated in other clusters (less than 11%). From this point of view, cluster 3 is in better agreement with the experiment[112] than other clusters.

Ahmed et al. also showed that the C-termini are buried inside the oligomer. Moreover, the Aβ_{18-41} tetramer structure obtained from a study by Streltsov et al. indicates that the C-termini constitute the core of the oligomer due to intermolecular contacts.[114] In our MD simulations, all clusters have a high intermolecular contact propensity at C-terminal residues (Figure 5). This result indicates the C-termini in our simulations located close to each other, which is consistent with experimental data.

Clusters 3 and 5 have lower nonbonded energy than 2NAO in both force fields. However, in the AMBER99SB-ILDN force field, the energy of cluster 5 is higher than cluster 3 (Figure 2). Therefore, cluster 3 is the most energetically stable in both force fields. Based on this result, cluster 3 seems to be the most probable structure of the Aβ42 tetramer because of its stability, and properties are in best agreement with experimental studies. Representative structures of the largest cluster, obtained in all-atom MD trajectories at equilibrium for cluster 3, are shown in Figure 7. These structures have three C-termini located close to each other, and they have a spheroid state but not rodlike shape.

3.15. Reasons why Tetramer Structure is Different from Fibril. Because the characteristics of the structure and arrangement of monomers in our tetramer models are different from four 2NAO chains, we investigated the total hydropathy index of residues forming interchain contacts in all-atom MD

DOI: 10.1021/acs.jpcb.9b04208
J. Phys. Chem. B XXXX, XXX, XXX−XXX

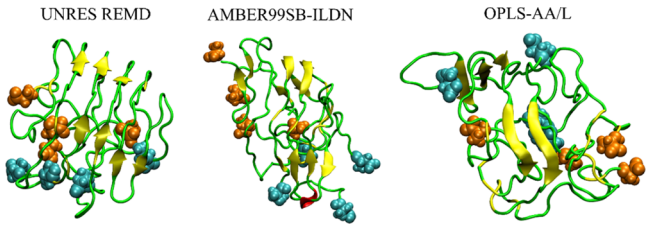

Figure 7. Representative structures of cluster 3 from UNRES REMD simulation and the largest cluster from five trajectories of all-atom MD simulations. Cyan balls represent the N-termini, and the orange balls represent the C-termini. The Cα-rmsd of structures from the MD simulation in AMBER99SB-ILDN and OPLS-AA/L force fields is 7.6 Å.

simulation, which allows us to estimate the hydropathy of the interface between monomers. In both AMBER and OPLS force fields, all clusters are more hydrophobic at the interface between monomers than 2NAO (Table 5) because of the larger values of the hydropathy index. Interestingly, cluster 3, which is the most probable structure of the Aβ42 tetramer, has the closest hydropathy to 2NAO than any other cluster in both force fields. This result is consistent with the hSASA values (Table 5) because cluster 3 has the largest hSASA value compared to other clusters. In addition, in AMBER, hSASA of cluster 3 is equivalent to 2NAO. The fact that the most probable tetrameric and fibril structures have low hydropathy of the contact interfaces between monomers indicates that a decrease in hydrophobic interactions at the interfaces of monomers may be a mechanism in the formation of fibril structures from oligomers.

Higher hydropathy values for our tetrameric structures than for 2NAO indicate which areas of the oligomer play an important role in the formation of tetramers and fibrils. The population of residues that form contacts during tetramer formation shows that in both tetramer formation processes 2 + 2 → 4 and 3 + 1 → 4, the C-terminus dominates the binding of monomers to a dimer or trimer to form a tetramer (Figure 8). This result is consistent with interchain contact results (Figure 5), in which the C-terminal region has high propensity to

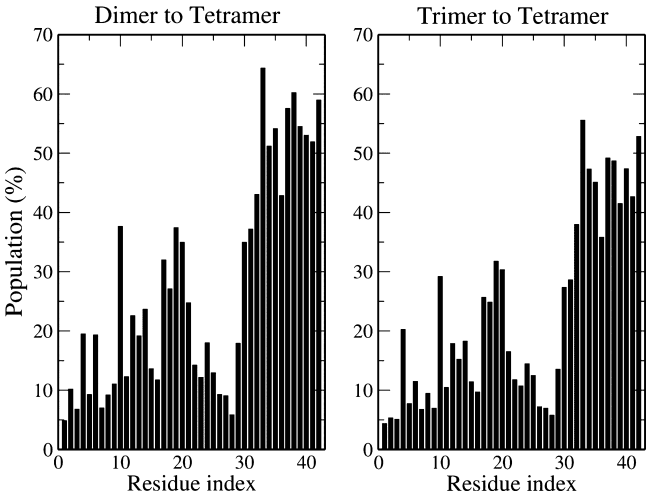

Figure 8. Population of interchain contacts between residues of dimer−dimer and trimer−monomer complexes, when a tetramer is formed from binding of two dimers or a trimer and a monomer. The result is obtained from all replicas of REMD simulation.

contacts. The number of residue pairs that form interchain contacts in our tetrameric structures (Figure 5) is larger than in the case of 2NAO (Figure S11). However, the interchain contact populations in our models are lower than in 2NAO. Because of the ordered structure, the interchain contact maps of 2NAO have high propensities along the diagonal elements, which are low in our tetrameric models. In 2NAO regions (30−42)−(30−42) and (13−20)−(30−42), there are significant populations of contacts, which is similar to our tetrameric models (Figure 5). These results suggest that in the beginning of the aggregation, the C-termini of monomers bind to each other and are located at or near the oligomer surface, while during the formation of the mature fibril, the monomers are aligned in the cross-beta structure with the C-termini out of the core.

Results, obtained for the interface hydrophobicity, prompted us to calculate the radial distribution of charged atoms in tetrameric models and 2NAO to explore the charge distribution in the fibril formation. In both force fields, charged fragments of tetrameric structures are located closer to the center of mass than in 2NAO (Figure 9) because the radial

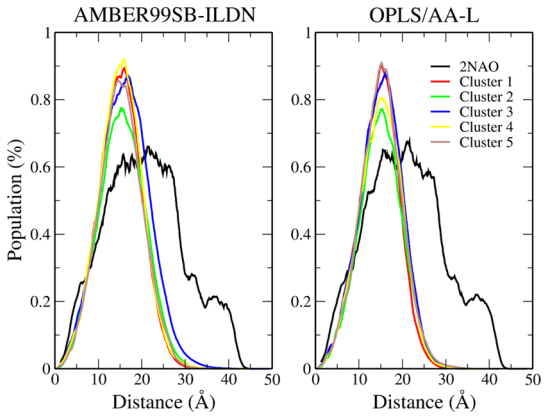

Figure 9. Distribution of distances between charged atoms and the center of mass of the tetramer from all-atom MD simulations.

distributions of charge are shifted to the lower values compared to 2NAO. This suggests that in tetrameric structures, charges are more focused inside, whereas in 2NAO, they are located near the surface of the fibrils. Therefore, the presence of repulsion forces between negatively charged monomers (−3e) leads to stretching the oligomer to keep the charges away from each other.

To better understand the role of the charge, we calculated the distribution of angles between the dipole moment and the principal inertia axes of tetramers and 2NAO (Figure S14). As evident from Figure 10, the distribution of three angles of 2NAO has a sharp peak in both force fields, while wide peaks occur in the case of five clusters. Cluster 1 even has two peaks in AMBER. Thus, the distribution of dipoles in tetrameric structures is more isotropic than in fibrils, which can be explained by the fact that the 2NAO structure is ordered, whereas our tetrameric structures are partially disordered.

The fibril formation changes not only the arrangement of hydrophobic residues and charges but also the number of water molecules located inside the tetramer. Therefore, we constructed concave hulls for the tetramers and counted the number of water molecules present in the resulting polyhedrons (Figure 11). The number of water molecules in

DOI: 10.1021/acs.jpcb.9b04208
J. Phys. Chem. B XXXX, XXX, XXX−XXX

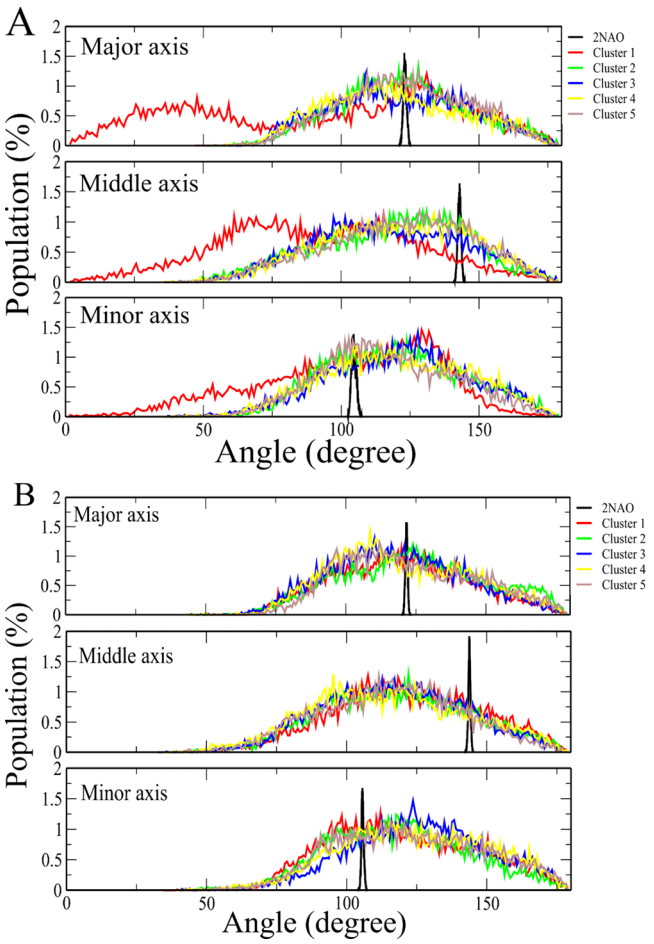

Figure 10. Distribution of angles between the dipole moment and three principal axes (major, middle, and minor) of inertial moment in AMBER99SB-ILDN (A) and OPLS/AA-L (B) force fields.

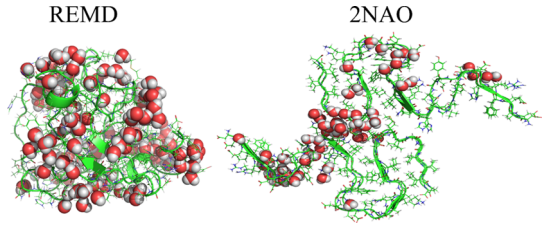

Figure 11. Schematic representation of the tetrameric Aβ42 structures with marked internal water molecules fitted into the constructed polyhedron.

2NAO is less than in our tetrameric models (Table 5). Therefore, the fibril is drier than the oligomer, implying that water molecules are ejected during the fibril formation process. Reddy and coworkers showed that water molecules are expulsed in the formation of the fibril of the Aβ C-terminal,[120] which is consistent with our results. Because the number of free water molecules in the solvent is increased with the fibril formation compared to oligomers, the water entropy is higher, which can compensate for the free energy required to form a fibril.

Based on abovementioned results, we propose that the fibril formation proceeds as follows: At the beginning, the hydrophobic region of the monomers will be tightly packed with each other forming a hydrophobic core. Because of the small size of the oligomer, only weak repulsive electrostatic interactions exist between Aβ42 chains (Figure 2) at this stage, and the charges can be distributed almost randomly. Because the interactions at this stage are mainly hydrophobic, which is manifested in the decisive contribution of vdW interactions to the total nonbonded energy of tetrameric structures (Figure 2), oligomers tend to form spheroid structures to minimize the solvent accessible area, which is reflected in hSASA results (Table 5). However, when the number of monomers in the aggregation state is large, the repulsive energy of long-range electrostatic interactions prevails over short-range vdW interactions of the hydrophobic interface between chains, which cause the structures to adopt unstable states. The monomers in the core of the spheroid oligomer will repel the monomers in the shell because the vdW interaction energy between them is small due to the large distance. Consequently, the spheroid shape of oligomers should change to minimize repulsion and optimize hydrophobic interactions in mature forms of aggregates. The charged residues move to the oligomer shell to reduce the internal repulsion energy, and the hydrophobic regions are more exposed to the solvent than to the oligomer to attract more monomers. This hypothesis is supported by the radial distribution of charges (Figure 9) and the higher hSASA values for 2NAO than for our models (Table 5). This statement is also confirmed by the analysis of the nonbonded energy components, which indicates that the fibril structure has more unfavorable internal Aβ interactions compared to our tetrameric models (Figure 2), while the solute−solvent interactions are more favorable for fibrils than oligomers in the AMBER force field, except cluster 1 (Figure 2). Moreover, fewer internal water molecules in four chains of 2NAO than in oligomer models (Table 5) indicate the movement of hydrophobic regions from the interior of the complex to the shell in the fibril formation.

Because the spheroid shape can compensate the repulsion between the core and the shell of the oligomer, as well as the binding of new Aβ chains to the oligomer, we hypothesize that the oligomers will be organized in lower dimensions to form mature fibrils. Monomers in the spheroid oligomer can repel new monomers from three dimensions (Figure 12) due to unfavorable electrostatic interactions. If the oligomers are arranged in the disc shape, the repulsive force acting on new monomers may decrease compared to three dimensions because the monomers in the oligomer are organized along the x and y axes (Figure 12). Finally, if the oligomers are organized in rodlike shape, new monomers are repelled only along one direction, namely, the x-axis (Figure 12), but they are strongly attracted by monomers at the end of the rodlike oligomer because of the vdW interactions. The electrostatic repulsion between monomers in the oligomer can be easily compensated by attractive vdW interactions between adjacent monomers. These interactions can be increased if the hydrophobic surface area at the interface of the aggregate is large, which attracts additional monomers to bind. Therefore, during the fibril formation, the monomers are regrouped to obtain a conformation in which hSASA is large and the electrostatic repulsion is weak. The energy required to increasing hSASA and the entropy contribution for the arrangement of monomers is positive, but they can be compensated for by reducing the electrostatic repulsion and increasing the water entropy due to the larger number of free water molecules. We assume that with an increase in the oligomer size, Aβ chains are organized in quasi-one dimension

DOI: 10.1021/acs.jpcb.9b04208
J. Phys. Chem. B XXXX, XXX, XXX−XXX

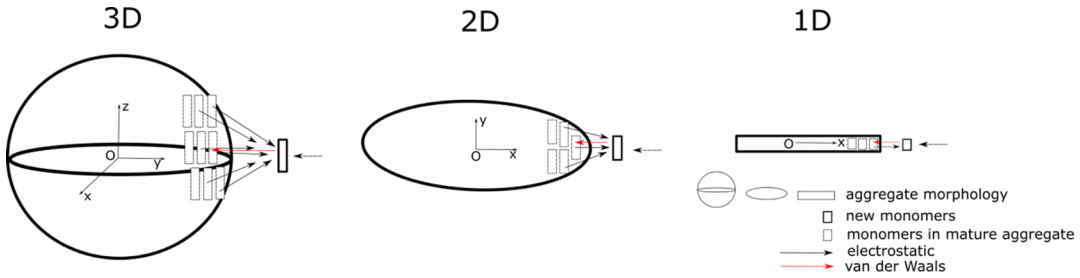

Figure 12. Schematic representation of fibril formation in 3, 2, and 1 dimensions in the left, middle, and right panel, respectively. In the 3D case, new monomers are under forces acted by monomers inside the oligomer along three directions *x*, *y*, and *z* because monomers are arranged in O_x, O_y, and O_z axes. Because the electrostatic interaction has a longer range than vdW interaction, the electrostatic interaction pushes new monomers out of oligomers before the attractive effect of vdW interaction begins to become significant. If the aggregate has a disc-like shape (2D), the electrostatic repulsion from the monomers inside the mature aggregate is reduced because it lacks monomers on the O_z axis. Then, if the aggregate has a rodlike shape, the repulsion is minimal, and the vdW interaction can attract new monomers more easily than in the 3D and 2D cases.

(e.g., in the form of a rod) and not in three dimensions (like a sphere), as in the case of small oligomers. Such a quasi-one-dimensional structure is consistent with many fibrillary structures reported in the literature.[27,29,30,32]

4. CONCLUSIONS

Using REMD simulation with a coarse-grained UNRES force field, we obtained five Aβ42 tetrameric structures, which were subsequently refined using MD simulations in two popular all-atom force fields. The most probable tetramer structures have a disc-like shape without a cross-beta structure. Moreover, the four chains in the tetramer are not equivalent to each other, most of the time two of them form the core, while other two are a shell that interacts weakly with other chains but much stronger with water molecules. For this reason, the observed β-content is lower for the oligomer than for fibrils. Our results indicate that structural rearrangement of the tetramer is necessary for the formation of higher order oligomers and fibril. The refined structures of cluster 3, obtained in this work, are in good agreement with experimental data, as well as with theoretical expectations and can be used, for example, as initial structures for constructing higher order oligomers or as targets for the development of AD medicines.

The charge distribution in our tetrameric models is more isotropic than in four chains taken from the fibril (PDB code: 2NAO). Furthermore, the hydrophobic regions in the fibril are more exposed to the solvent than in the oligomer. Consequently, the water density inside the oligomer is higher than in fibrils, and this may be related to the enhanced toxicity of oligomers. Based on the difference between our tetrameric models and the 2NAO structure, we hypothesize that during the fibril formation, the repulsion between monomers in the core of spheroid oligomers is the main cause of the lower stability of oligomeric conformations. Therefore, upon fibril formation, they reorganize the structure to adopt a quasi-one-dimensional or rodlike shape in order to minimize the repulsion of the Aβ42 chains and optimize the attraction between neighboring chains.

It has to be noted that results presented in this work are valid only for water environment and Aβ structures and dynamics can significantly vary in different environments (e.g., SDS)[121] or water−lipid interface.[122] The latter seems to play an important role in AD development,[123] and such studies are currently undergoing in our lab.

■ ASSOCIATED CONTENT

Supporting Information

The Supporting Information is available free of charge on the ACS Publications website at DOI: 10.1021/acs.jpcb.9b04208.

All-atom structures of five clusters (ZIP)

rmsd of docking structures with structure 1 is the reference structure; Cα-rmsd (Å) between representative structures from all-atom MD simulations and the representative structures from coarse-grained REMD simulation; average secondary structure of all chains in MD simulations; initial structures in UNRES REMD simulation; walk of replica 1 and 24 in REMD simulation; number of interchain contact histogram in REMD simulation; distribution of oligomer size in UNRES REMD simulation; Cα-rmsd of all-atom MD trajectories; representative structures from all-atom MD simulations starting from the structures obtained in the UNRES REMD simulation; secondary structure distributions from all-atom MD simulations starting from UNRES structures with AMBER99SB-ILDN and OPLS force fields presented separately for each chain; RMSF of the tetramer from all-atom MD simulations starting from UNRES structures with the AMBER99-ILDN force field presented separately for each chain; initial structure for each simulation was used as the reference; contact map (distance of center of mass between two side chains below 6.5 Å) within each chain, calculated from all-atom MD simulations in AMBER99-ILDN and OPLS force fields starting from UNRES structures; transition networks of REMD coarse-grained and conventional all-atom simulations; interchain contact map of 2NAO from all-atom MD simulation; schematic plot for dipole moment and inertia principal axes (PDF)

■ AUTHOR INFORMATION

Corresponding Author

*E-mail: masli@ifpan.edu.pl. Phone: +48 22 843 66 01.

ORCID

Mai Suan Li: 0000-0001-7021-7916

Author Contributions

M.S.L. conceived the experiments. N.H.L., P.K., and N.M.H. conducted the experiment. N.H.L., P.K., N.M.H., and M.S.L. analyzed the results. M.S.L., P.K., and N.H.L. wrote the paper. All the authors reviewed the manuscript.

DOI: 10.1021/acs.jpcb.9b04208
J. Phys. Chem. B XXXX, XXX, XXX−XXX

Funding

This work was supported by Narodowe Centrum Nauki in Poland (grant nos. 2015/19/B/ST4/02721 and 2017/27/N/NZ1/02871) and Department of Science and Technology at Ho Chi Minh City, Vietnam (grant no. 03/2018/HD-KHCNTT). Allocation of CPU time at the supercomputer center TASK in Gdansk (Poland) is highly appreciated. This research was also supported in part by PLGrid Infrastructure in Poland.

Notes

The authors declare no competing financial interest.

REFERENCES

(1) Qiu, C.; Kivipelto, M.; von Strauss, E. Epidemiology of Alzheimer's disease: occurrence, determinants, and strategies toward intervention. *Dialogues Clin. Neurosci.* **2009**, *11*, 111−128.

(2) Serrano-Pozo, A.; Frosch, M. P.; Masliah, E.; Hyman, B. T. Neuropathological Alterations in Alzheimer Disease. *Cold Spring Harbor Perspect. Med.* **2011**, *1*, a006189.

(3) Chiti, F.; Dobson, C. M. Protein Misfolding, Amyloid Formation, and Human Disease: A Summary of Progress over the Last Decade. *Annu. Rev. Biochem.* **2017**, *86*, 27−68.

(4) Braak, H.; Zetterberg, H.; Del Tredici, K.; Blennow, K. Intraneuronal tau aggregation precedes diffuse plaque deposition, but amyloid-β changes occur before increases of tau in cerebrospinal fluid. *Acta Neuropathol.* **2013**, *126*, 631−641.

(5) Bloom, G. S. Amyloid-β and Tau. *JAMA Neurol.* **2014**, *71*, 505−508.

(6) Buchhave, P.; Minthon, L.; Zetterberg, H.; Wallin, Å. K.; Blennow, K.; Hansson, O. Cerebrospinal Fluid Levels of β-Amyloid 1-42, but Not of Tau, Are Fully Changed Already 5 to 10 Years Before the Onset of Alzheimer Dementia. *Annu. Rev. Biochem.* **2012**, *69*, 98−106.

(7) Chow, V. W.; Mattson, M. P.; Wong, P. C.; Gleichmann, M. An Overview of App Processing Enzymes and Products. *NeuroMol. Med.* **2010**, *12*, 1−12.

(8) Suzuki, N.; Cheung, T.; Cai, X.; Odaka, A.; Otvos, L., Jr.; Eckman, C.; Golde, T.; Younkin, S. An increased percentage of long amyloid beta protein secreted by familial amyloid beta protein precursor (beta APP717) mutants. *Science* **1994**, *264*, 1336−1340.

(9) Jarrett, J. T.; Berger, E. P.; Lansbury, P. T., Jr. The carboxy terminus of the .beta. amyloid protein is critical for the seeding of amyloid formation: Implications for the pathogenesis of Alzheimer's disease. *Biochemistry* **1993**, *32*, 4693−4697.

(10) El-Agnaf, O. M. A.; Mahil, D. S.; Patel, B. P.; Austen, B. M. Oligomerization and Toxicity of β-Amyloid-42 Implicated in Alzheimer's Disease. *Biochem. Biophys. Res. Commun.* **2000**, *273*, 1003−1007.

(11) Riek, R.; Güntert, P.; Döbeli, H.; Wipf, B.; Wüthrich, K. NMR studies in aqueous solution fail to identify significant conformational differences between the monomeric forms of two Alzheimer peptides with widely different plaque-competence, Aβ(1-0)(ox) and Aβ(1-42)(ox). *FEBS J.* **2001**, *268*, 5930−5936.

(12) Hou, L.; Shao, H.; Zhang, Y.; Li, H.; Menon, N. K.; Neuhaus, E. B.; Brewer, J. M.; Byeon, I.-J. L.; Ray, D. G.; Vitek, M. P.; Iwashita, T.; Makula, R. A.; Przybyla, A. B.; Zagorski, M. G. Solution NMR Studies of the Aβ(1−40) and Aβ(1−42) Peptides Establish that the Met35 Oxidation State Affects the Mechanism of Amyloid Formation. *J. Am. Chem. Soc.* **2004**, *126*, 1992−2005.

(13) Aleksis, R.; Oleskovs, F.; Jaudzems, K.; Pahnke, J.; Biverstål, H. Structural studies of amyloid-β peptides: Unlocking the mechanism of aggregation and the associated toxicity. *Biochimie* **2017**, *140*, 176−192.

(14) Hardy, J.; Selkoe, D. J. The Amyloid Hypothesis of Alzheimer's Disease: Progress and Problems on the Road to Therapeutics. *Science* **2002**, *297*, 353−356.

(15) Cappai, R.; Barnham, K. J. Delineating the Mechanism of Alzheimer's Disease Aβ Peptide Neurotoxicity. *Neurochem. Res.* **2008**, *33*, 526−532.

(16) Baglioni, S.; Casamenti, F.; Bucciantini, M.; Luheshi, L. M.; Taddei, N.; Chiti, F.; Dobson, C. M.; Stefani, M. Prefibrillar Amyloid Aggregates Could Be Generic Toxins in Higher Organisms. *J. Neurosci.* **2006**, *26*, 8160−8167.

(17) Haass, C.; Selkoe, D. J. Soluble protein oligomers in neurodegeneration: lessons from the Alzheimer's amyloid β-peptide. *Nat. Rev. Mol. Cell Biol.* **2007**, *8*, 101.

(18) McLean, C. A.; Cherny, R. A.; Fraser, F. W.; Fuller, S. J.; Smith, M. J.; Konrad Vbeyreuther, A. I.; Bush, A. I.; Masters, C. L. Soluble pool of A beta amyloid as a determinant of severity of neurodegeneration in Alzheimer's disease. *Ann. Neurol.* **1999**, *46*, 860−866.

(19) Cleary, J. P.; Walsh, D. M.; Hofmeister, J. J.; Shankar, G. M.; Kuskowski, M. A.; Selkoe, D. J.; Ashe, K. H. Natural oligomers of the amyloid-β protein specifically disrupt cognitive function. *Nat. Neurosci.* **2005**, *8*, 79.

(20) Serra-Batiste, M.; Ninot-Pedrosa, M.; Bayoumi, M.; Gairí, M.; Maglia, G.; Carulla, N. Aβ42 assembles into specific β-barrel pore-forming oligomers in membrane-mimicking environments. *Proc. Natl. Acad. Sci. U.S.A.* **2016**, *113*, 10866−10871.

(21) Lee, J.; Kim, Y. H.; Arce, F. T.; Gillman, A. L.; Jang, H.; Kagan, B. L.; Nussinov, R.; Yang, J.; Lal, R. Amyloid β Ion Channels in a Membrane Comprising Brain Total Lipid Extracts. *ACS Chem. Neurosci.* **2017**, *8*, 1348−1357.

(22) Drews, A.; Flint, J.; Shivji, N.; Jönsson, P.; Wirthensohn, D.; De Genst, E.; Vincke, C.; Muyldermans, S.; Dobson, C.; Klenerman, D. Individual Aggregates of Amyloid Beta Induce Temporary Calcium Influx through the Cell Membrane of Neuronal Cells. *Sci. Rep.* **2016**, *6*, 31910.

(23) Yang, T.; Li, S.; Xu, H.; Walsh, D. M.; Selkoe, D. J. Large Soluble Oligomers of Amyloid β-Protein from Alzheimer Brain Are Far Less Neuroactive Than the Smaller Oligomers to Which They Dissociate. *J. Neurosci.* **2017**, *37*, 152−163.

(24) Jana, M. K.; Cappai, R.; Pham, C. L. L.; Ciccotosto, G. D. Membrane-bound tetramer and trimer Aβ oligomeric species correlate with toxicity towards cultured neurons. *J. Neurochem.* **2016**, *136*, 594−608.

(25) Ono, K.; Condron, M. M.; Teplow, D. B. Structure-neurotoxicity relationships of amyloid -protein oligomers. *Proc. Natl. Acad. Sci. U.S.A.* **2009**, *106*, 14745−14750.

(26) Xiao, Y.; Ma, B.; McElheny, D.; Parthasarathy, S.; Long, F.; Hoshi, M.; Nussinov, R.; Ishii, Y. Aβ(1-42) fibril structure illuminates self-recognition and replication of amyloid in Alzheimer's disease. *Nat. Struct. Mol. Biol.* **2015**, *22*, 499.

(27) Wälti, M. A.; Ravotti, F.; Arai, H.; Glabe, C. G.; Wall, J. S.; Böckmann, A.; Güntert, P.; Meier, B. H.; Riek, R. Atomic-resolution structure of a disease-relevant Aβ(1-42) amyloid fibril. *Proc. Natl. Acad. Sci. U.S.A.* **2016**, *113*, E4976−E4984.

(28) Colvin, M. T.; Silvers, R.; Ni, Q. Z.; Can, T. V.; Sergeyev, I.; Rosay, M.; Donovan, K. J.; Michael, B.; Wall, J.; Linse, S.; Griffin, R. G. Atomic Resolution Structure of Monomorphic Aβ42 Amyloid Fibrils. *J. Am. Chem. Soc.* **2016**, *138*, 9663−9674.

(29) Gremer, L.; Schölzel, D.; Schenk, C.; Reinartz, E.; Labahn, J.; Ravelli, R. B. G.; Tusche, M.; Lopez-Iglesias, C.; Hoyer, W.; Heise, H.; Willbold, D.; Schröder, G. F. Fibril structure of amyloid-β(1-42) by cryo-electron microscopy. *Science* **2017**, *358*, 116−119.

(30) Lu, J.-X.; Qiang, W.; Yau, W.-M.; Schwieters, C. D.; Meredith, S. C.; Tycko, R. Molecular Structure of β-Amyloid Fibrils in Alzheimer's Disease Brain Tissue. *Cell* **2013**, *154*, 1257−1268.

(31) Nasica-Labouze, J.; Nguyen, P. H.; Sterpone, F.; Berthoumieu, O.; Buchete, N.-V.; Coté, S.; De Simone, A.; Doig, A. J.; Faller, P.; Garcia, A.; Laio, A.; Li, M. S.; Melchionna, S.; Mousseau, N.; Mu, Y.; Paravastu, A.; Pasquali, S.; Rosenman, D. J.; Strodel, B.; Tarus, B.; Viles, J. H.; Zhang, T.; Wang, C.; Derreumaux, P. Amyloid β Protein and Alzheimer's Disease: When Computer Simulations Complement Experimental Studies. *Chem. Rev.* **2015**, *115*, 3518−3563.

DOI: 10.1021/acs.jpcb.9b04208
J. Phys. Chem. B XXXX, XXX, XXX−XXX

(32) Luhrs, T.; Ritter, C.; Adrian, M.; Riek-Loher, D.; Bohrmann, B.; Dobeli, H.; Schubert, D.; Riek, R. 3D structure of Alzheimer's amyloid- (1-42) fibrils. *Proc. Natl. Acad. Sci. U.S.A.* **2005**, *102*, 17342−17347.
(33) Qiang, W.; Yau, W.-M.; Luo, Y.; Mattson, M. P.; Tycko, R. Antiparallel -sheet architecture in Iowa-mutant -amyloid fibrils. *Proc. Natl. Acad. Sci. U.S.A.* **2012**, *109*, 4443−4448.
(34) Chandra, B.; Bhowmik, D.; Maity, B. K.; Mote, K. R.; Dhara, D.; Venkatramani, R.; Maiti, S.; Madhu, P. K. Major Reaction Coordinates Linking Transient Amyloid-β Oligomers to Fibrils Measured at Atomic Level. *Biophys. J.* **2017**, *113*, 805−816.
(35) Yu, L.; Edalji, R.; Harlan, J. E.; Holzman, T. F.; Lopez, A. P.; Labkovsky, B.; Hillen, H.; Barghorn, S.; Ebert, U.; Richardson, P. L.; Miesbauer, L.; Solomon, L.; Bartley, D.; Walter, K.; Johnson, R. W.; Hajduk, P. J.; Olejniczak, E. T. Structural Characterization of a Soluble Amyloid β-Peptide Oligomer. *Biochemistry* **2009**, *48*, 1870−1877.
(36) Yang, M.; Teplow, D. B. Amyloid β-Protein Monomer Folding: Free-Energy Surfaces Reveal Alloform-Specific Differences. *J. Mol. Biol.* **2008**, *384*, 450−464.
(37) Linh, N. H.; Tran, T. T. M.; Tu, L.; Hu, C.-K.; Li, M. S. Impact of Mutations at C-Terminus on Structures and Dynamics of Aβ40 and Aβ42: Molecular Simulation Study. *J. Phys. Chem. B* **2017**, *121*, 4341−4354.
(38) Truong, P. M.; Viet, M. H.; Nguyen, P. H.; Hu, C.-K.; Li, M. S. Effect of Taiwan Mutation (D7H) on Structures of Amyloid-β Peptides: Replica Exchange Molecular Dynamics Study. *J. Phys. Chem. B* **2014**, *118*, 8972−8981.
(39) Nguyen, H. L.; Thi Minh Thu, T.; Truong, P. M.; Lan, P. D.; Man, V. H.; Nguyen, P. H.; Tu, L. A.; Chen, Y.-C.; Li, M. S. Aβ41 Aggregates More Like Aβ40 than Like Aβ42: In Silico and in Vitro Study. *J. Phys. Chem. B* **2016**, *120*, 7371−7379.
(40) Zhang, Y.; Hashemi, M.; Lv, Z.; Lyubchenko, Y. L. Self-assembly of the full-length amyloid Aβ42 protein in dimers. *Nanoscale* **2016**, *8*, 18928−18937.
(41) Liao, Q.; Owen, M. C.; Bali, S.; Barz, B.; Strodel, B. Aβ under stress: the effects of acidosis, Cu2+-binding, and oxidation on amyloid β-peptide dimers. *Chem. Commun.* **2018**, *54*, 7766−7769.
(42) Cao, Y.; Jiang, X.; Han, W. Self-Assembly Pathways of β-Sheet-Rich Amyloid-β(1-40) Dimers: Markov State Model Analysis on Millisecond Hybrid-Resolution Simulations. *J. Chem. Theory Comput.* **2017**, *13*, 5731−5744.
(43) Zhang, T.; Zhang, J.; Derreumaux, P.; Mu, Y. Molecular Mechanism of the Inhibition of EGCG on the Alzheimer Aβ1-42 Dimer. *J. Phys. Chem. B* **2013**, *117*, 3993−4002.
(44) Zhu, X.; Bora, R. P.; Barman, A.; Singh, R.; Prabhakar, R. Dimerization of the Full-Length Alzheimer Amyloid β-Peptide (Aβ42) in Explicit Aqueous Solution: A Molecular Dynamics Study. *J. Phys. Chem. B* **2012**, *116*, 4405−4416.
(45) Chong, S.-H.; Ham, S. Atomic-level investigations on the amyloid-β dimerization process and its driving forces in water. *Phys. Chem. Chem. Phys.* **2012**, *14*, 1573−1575.
(46) Barz, B.; Urbanc, B. Dimer Formation Enhances Structural Differences between Amyloid β-Protein (1-40) and (1-42): An Explicit-Solvent Molecular Dynamics Study. *PLoS One* **2012**, *7*, No. e34345.
(47) Tarus, B.; Tran, T. T.; Nasica-Labouze, J.; Sterpone, F.; Nguyen, P. H.; Derreumaux, P. Structures of the Alzheimer's Wild-Type Aβ1-40 Dimer from Atomistic Simulations. *J. Phys. Chem. B* **2015**, *119*, 10478−10487.
(48) Nagel-Steger, L.; Owen, M. C.; Strodel, B. An Account of Amyloid Oligomers: Facts and Figures Obtained from Experiments and Simulations. *ChemBioChem* **2016**, *17*, 657−676.
(49) Brown, A. M.; Bevan, D. R. Molecular Dynamics Simulations of Amyloid β -Peptide (1-42): Tetramer Formation and Membrane Interactions. *Biophys. J.* **2016**, *111*, 937−949.
(50) Meral, D.; Urbanc, B. Discrete Molecular Dynamics Study of Oligomer Formation by N-Terminally Truncated Amyloid β-Protein. *J. Mol. Biol.* **2013**, *425*, 2260−2275.
(51) Barz, B.; Olubiyi, O. O.; Strodel, B. Early amyloid β-protein aggregation precedes conformational change. *Chem. Commun.* **2014**, *50*, 5373−5375.
(52) Barz, B.; Liao, Q.; Strodel, B. Pathways of Amyloid-β Aggregation Depend on Oligomer Shape. *J. Am. Chem. Soc.* **2018**, *140*, 319−327.
(53) Chebaro, Y.; Jiang, P.; Zang, T.; Mu, Y.; Nguyen, P. H.; Mousseau, N.; Derreumaux, P. Structures of Aβ17-42 Trimers in Isolation and with Five Small-Molecule Drugs Using a Hierarchical Computational Procedure. *J. Phys. Chem. B* **2012**, *116*, 8412−8422.
(54) Kim, S.; Takeda, T.; Klimov, D. K. Mapping Conformational Ensembles of Aβ Oligomers in Molecular Dynamics Simulations. *Biophys. J.* **2010**, *99*, 1949−1958.
(55) Liwo, A.; Ołdziej, S.; Pincus, M. R.; Wawak, R. J.; Rackovsky, S.; Scheraga, H. A. A united-residue force field for off-lattice protein-structure simulations. I. Functional forms and parameters of long-range side-chain interaction potentials from protein crystal data. *J. Comput. Chem.* **1997**, *18*, 849−873.
(56) Khalili, M.; Liwo, A.; Jagielska, A.; Scheraga, H. A. Molecular Dynamics with the United-Residue Model of Polypeptide Chains. II. Langevin and Berendsen-Bath Dynamics and Tests on Model α-Helical Systems. *J. Phys. Chem. B* **2005**, *109*, 13798−13810.
(57) Nanias, M.; Czaplewski, C.; Scheraga, H. A. Replica Exchange and Multicanonical Algorithms with the Coarse-Grained United-Residue (Unres) Force Field. *J. Chem. Theory Comput.* **2006**, *2*, 513−528.
(58) Rojas, A. V.; Liwo, A.; Scheraga, H. A. Molecular Dynamics with the United-Residue Force Field: Ab Initio Folding Simulations of Multichain Proteins. *J. Phys. Chem. B* **2007**, *111*, 293−309.
(59) Petkova, A. T.; Yau, W.-M.; Tycko, R. Experimental Constraints on Quaternary Structure in Alzheimer's β-Amyloid Fibrils†. *Biochemistry* **2006**, *45*, 498−512.
(60) Kim, Y. S.; Liu, L.; Axelsen, P. H.; Hochstrasser, R. M. 2D IR provides evidence for mobile water molecules in -amyloid fibrils. *Proc. Natl. Acad. Sci. U.S.A.* **2009**, *106*, 17751−17756.
(61) Wang, T.; Jo, H.; DeGrado, W. F.; Hong, M. Water Distribution, Dynamics, and Interactions with Alzheimer's β-Amyloid Fibrils Investigated by Solid-State NMR. *J. Am. Chem. Soc.* **2017**, *139*, 6242−6252.
(62) Xi, W.; Hansmann, U. H. E. Ring-Like N-Fold Models of a Beta(42) Fibrils. *Sci. Rep.* **2017**, *7*, 6588.
(63) Kozakov, D.; Beglov, D.; Bohnuud, T.; Mottarella, S. E.; Xia, B.; Hall, D. R.; Vajda, S. How Good Is Automated Protein Docking? *Proteins: Struct., Funct., Bioinf.* **2013**, *81*, 2159−2166.
(64) Kozakov, D.; Hall, D. R.; Xia, B.; Porter, K. A.; Padhorny, D.; Yueh, C.; Beglov, D.; Vajda, S. The Cluspro Web Server for Protein-Protein Docking. *Nat. Protoc.* **2017**, *12*, 255−278.
(65) Liwo, A.; Baranowski, M.; Czaplewski, C.; Gołaś, E.; He, Y.; Jagieła, D.; Krupa, P.; Maciejczyk, M.; Makowski, M.; Mozolewska, M. A. A Unified Coarse-Grained Model of Biological Macromolecules Based on Mean-Field Multipole−Multipole Interactions. *J. Mol. Model.* **2014**, *20*, 2306.
(66) Sieradzan, A. K.; Krupa, P.; Scheraga, H. A.; Liwo, A.; Czaplewski, C. Physics-Based Potentials for the Coupling between Backbone- and Side-Chain-Local Conformational States in the United Residue (UNRES) Force Field for Protein Simulations. *J. Chem. Theory Comput.* **2015**, *11*, 817−831.
(67) Krupa, P.; Hałabis, A.; Żmudzińska, W.; Ołdziej, S.; Scheraga, H. A.; Liwo, A. Maximum Likelihood Calibration of the Unres Force Field for Simulation of Protein Structure and Dynamics. *J. Chem. Inf. Model.* **2017**, *57*, 2364−2377.
(68) Sieradzan, A. K. Introduction of Periodic Boundary Conditions into Unres Force Field. *J. Comput. Chem.* **2015**, *36*, 940−946.
(69) Mozolewska, M. A.; Krupa, P.; Scheraga, H. A.; Liwo, A. Molecular modeling of the binding modes of the iron-sulfur protein to the Jac1 co-chaperone fromSaccharomyces cerevisiaeby all-atom and coarse-grained approaches. *Proteins: Struct., Funct., Bioinf.* **2015**, *83*, 1414−1426.

DOI: 10.1021/acs.jpcb.9b04208
J. Phys. Chem. B XXXX, XXX, XXX−XXX

(70) Krupa, P.; Mozolewska, M. A.; Wiśniewska, M.; Yin, Y.; He, Y.; Sieradzan, A. K.; Ganzynkowicz, R.; Lipska, A. G.; Karczyńska, A.; Ślusarz, M.; Ślusarz, R.; Giełdoń, A.; Czaplewski, C.; Jagieła, D.; Zaborowski, B.; Scheraga, H. A.; Liwo, A. Performance of Protein-Structure Predictions with the Physics-Based Unres Force Field in Casp11. *Bioinformatics* **2016**, *32*, 3270−3278.
(71) Maisuradze, G. G.; Medina, J.; Kachlishvili, K.; Krupa, P.; Mozolewska, M. A.; Martin-Malpartida, P.; Maisuradze, L.; Macias, M. J.; Scheraga, H. A. Preventing Fibril Formation of a Protein by Selective Mutation. *Proc. Natl. Acad. Sci. U.S.A.* **2015**, *112*, 13549−13554.
(72) Rojas, A.; Liwo, A.; Browne, D.; Scheraga, H. A. Mechanism of Fiber Assembly: Treatment of Aβ Peptide Aggregation with a Coarse-Grained United-Residue Force Field. *J. Mol. Biol.* **2010**, *404*, 537−552.
(73) Rojas, A.; Maisuradze, N.; Kachlishvili, K.; Scheraga, H. A.; Maisuradze, G. G. Elucidating Important Sites and the Mechanism for Amyloid Fibril Formation by Coarse-Grained Molecular Dynamics. *ACS Chem. Neurosci.* **2016**, *8*, 201−209.
(74) Doig, A. J.; del Castillo-Frias, M. P.; Berthoumieu, O.; Tarus, B.; Nasica-Labouze, J.; Sterpone, F.; Nguyen, P. H.; Hooper, N. M.; Faller, P.; Derreumaux, P. Why Is Research on Amyloid-β Failing to Give New Drugs for Alzheimer's Disease? *ACS Chem. Neurosci.* **2017**, *8*, 1435−1437.
(75) Kmiecik, S.; Gront, D.; Kolinski, M.; Wieteska, L.; Dawid, A. E.; Kolinski, A. Coarse-Grained Protein Models and Their Applications. *Chem. Rev.* **2016**, *116*, 7898−7936.
(76) Kumar, S.; Rosenberg, J. M.; Bouzida, D.; Swendsen, R. H.; Kollman, P. A. THE weighted histogram analysis method for free-energy calculations on biomolecules. I. The method. *J. Comput. Chem.* **1992**, *13*, 1011−1021.
(77) Liwo, A.; Khalili, M.; Czaplewski, C.; Kalinowski, S.; Ołdziej, S.; Wachucik, K.; Scheraga, H. A. Modification and Optimization of the United-Residue (Unres) Potential Energy Function for Canonical Simulations. I. Temperature Dependence of the Effective Energy Function and Tests of the Optimization Method with Single Training Proteins. *J. Phys. Chem. B* **2007**, *111*, 260−285.
(78) Murtagh, F.; Heck, A. *Book Review: Multivariate Data Analysis*; Kluwer Academic, 1986; Observatory 1987, Vol. *107*, p 227.
(79) Abraham, M. J.; Murtola, T.; Schulz, R.; Páll, S.; Smith, J. C.; Hess, B.; Lindahl, E. Gromacs: High Performance Molecular Simulations through Multi-Level Parallelism from Laptops to Supercomputers. *SoftwareX* **2015**, *1-2*, 19−25.
(80) Darden, T.; York, D.; Pedersen, L. Particle mesh Ewald: An N·log(N) method for Ewald sums in large systems. *J. Chem. Phys.* **1993**, *98*, 10089−10092.
(81) Hess, B.; Bekker, H.; Berendsen, H. J. C.; Fraaije, J. G. E. M. Lincs: A Linear Constraint Solver for Molecular Simulations. *J. Comput. Chem.* **1997**, *18*, 1463−1472.
(82) Rotkiewicz, P.; Skolnick, J. Fast procedure for reconstruction of full-atom protein models from reduced representations. *J. Comput. Chem.* **2008**, *29*, 1460−1465.
(83) Krivov, G. G.; Shapovalov, M. V.; Dunbrack, R. L. Improved prediction of protein side-chain conformations with SCWRL4. *Proteins: Struct., Funct., Bioinf.* **2009**, *77*, 778−795.
(84) Lindorff-Larsen, K.; Piana, S.; Palmo, K.; Maragakis, P.; Klepeis, J. L.; Dror, R. O.; Shaw, D. E. Improved Side-Chain Torsion Potentials for the Amber Ff99sb Protein Force Field. *Proteins: Struct., Funct., Bioinf.* **2010**, *78*, 1950−1958.
(85) Kaminski, G. A.; Friesner, R. A.; Tirado-Rives, J.; Jorgensen, W. L. Evaluation and Reparametrization of the OPLS-AA Force Field for Proteins via Comparison with Accurate Quantum Chemical Calculations on Peptides†. *J. Phys. Chem. B* **2001**, *105*, 6474−6487.
(86) Jorgensen, W. L.; Chandrasekhar, J.; Madura, J. D.; Impey, R. W.; Klein, M. L. Comparison of Simple Potential Functions for Simulating Liquid Water. *J. Chem. Phys.* **1983**, *79*, 926−935.
(87) Man, V. H.; Nguyen, P. H.; Derreumaux, P. High-Resolution Structures of the Amyloid-β 1-42 Dimers from the Comparison of Four Atomistic Force Fields. *J. Phys. Chem. B* **2017**, *121*, 5977−5987.
(88) Gerben, S. R.; Lemkul, J. A.; Brown, A. M.; Bevan, D. R. Comparing atomistic molecular mechanics force fields for a difficult target: a case study on the Alzheimer's amyloid β-peptide. *J. Biomol. Struct. Dyn.* **2014**, *32*, 1817−1832.
(89) Somavarapu, A. K.; Kepp, K. P. The Dependence of Amyloid-β Dynamics on Protein Force Fields and Water Models. *ChemPhysChem* **2015**, *16*, 3278−3289.
(90) Carballo-Pacheco, M.; Strodel, B. Comparison of Force Fields for Alzheimer's A: A Case Study for Intrinsically Disordered Proteins. *Protein Sci.* **2017**, *26*, 174−185.
(91) Bussi, G.; Donadio, D.; Parrinello, M. Canonical Sampling through Velocity Rescaling. *J. Chem. Phys.* **2007**, *126*, 014101.
(92) Frishman, D.; Argos, P. Knowledge-based protein secondary structure assignment. *Proteins: Struct., Funct., Bioinf.* **1995**, *23*, 566−579.
(93) Kyte, J.; Doolittle, R. F. A Simple Method for Displaying the Hydropathic Character of a Protein. *J. Mol. Biol.* **1982**, *157*, 105−132.
(94) Barber, C. B.; Dobkin, D. P.; Huhdanpaa, H. The Quickhull Algorithm for Convex Hulls. *ACM Trans. Math Software* **1996**, *22*, 469−483.
(95) Park, J.-S.; Oh, S.-J. A New Concave Hull Algorithm and Concaveness Measure for N-Dimensional Datasets. *J. Inf. Sci. Eng.* **2012**, *28*, 587−600.
(96) Daura, X.; Gademann, K.; Jaun, B.; Seebach, D.; van Gunsteren, W. F.; Mark, A. E. Peptide Folding: When Simulation Meets Experiment. *Angew. Chem., Int. Ed.* **1999**, *38*, 236−240.
(97) Riccardi, L.; Nguyen, P. H.; Stock, G. Construction of the Free Energy Landscape of Peptide Aggregation from Molecular Dynamics Simulations. *J. Chem. Theory Comput.* **2012**, *8*, 1471−1479.
(98) Barz, B.; Wales, D. J.; Strodel, B. A Kinetic Approach to the Sequence-Aggregation Relationship in Disease-Related Protein Assembly. *J. Phys. Chem. B* **2014**, *118*, 1003−1011.
(99) Bastian, M.; Heymann, S.; Jacomy, M. *Gephi: An Open Source Software for Exploring and Manipulating Networks*; ICWSM, 2009; Vol. *8*, pp 361−362.
(100) Mesleh, M. F.; Hunter, J. M.; Shvartsburg, A. A.; Schatz, G. C.; Jarrold, M. F. Structural Information from Ion Mobility Measurements: Effects of the Long-Range Potential. *J. Phys. Chem.* **1996**, *100*, 16082−16086.
(101) Shvartsburg, A. A.; Jarrold, M. F. An Exact Hard-Spheres Scattering Model for the Mobilities of Polyatomic Ions. *Chem. Phys. Lett.* **1996**, *261*, 86−91.
(102) May, J. C.; Morris, C. B.; McLean, J. A. Ion Mobility Collision Cross Section Compendium. *Anal. Chem.* **2016**, *89*, 1032−1044.
(103) Eisenhaber, F.; Lijnzaad, P.; Argos, P.; Sander, C.; Scharf, M. The Double Cubic Lattice Method: Efficient Approaches to Numerical Integration of Surface Area and Volume and to Dot Surface Contouring of Molecular Assemblies. *J. Comput. Chem.* **1995**, *16*, 273−284.
(104) Sengupta, U.; Carballo-Pacheco, M.; Strodel, B. Automated Markov State Models for Molecular Dynamics Simulations of Aggregation and Self-Assembly. *J. Chem. Phys.* **2019**, *150*, 115101.
(105) Strodel, B.; Whittleston, C. S.; Wales, D. J. Thermodynamics and Kinetics of Aggregation for the Gnnqqny Peptide. *J. Am. Chem. Soc.* **2007**, *129*, 16005−16014.
(106) Pham, J. D.; Chim, N.; Goulding, C. W.; Nowick, J. S. Structures of Oligomers of a Peptide from β-Amyloid. *J. Am. Chem. Soc.* **2013**, *135*, 12460−12467.
(107) Laganowsky, A.; Liu, C.; Sawaya, M. R.; Whitelegge, J. P.; Park, J.; Zhao, M.; Pensalfini, A.; Soriaga, A. B.; Landau, M.; Teng, P. K.; et al. Atomic View of a Toxic Amyloid Small Oligomer. *Science* **2012**, *335*, 1228−1231.
(108) Berhanu, W. M.; Hansmann, U. H. E. The stability of cylindrin β-barrel amyloid oligomer models-A molecular dynamics study. *Proteins: Struct., Funct., Bioinf.* **2013**, *81*, 1542−1555.
(109) Haupt, C.; Leppert, J.; Rönicke, R.; Meinhardt, J.; Yadav, J. K.; Ramachandran, R.; Ohlenschläger, O.; Reymann, K. G.; Görlach, M.; Fändrich, M. Structural Basis of β-Amyloid-Dependent Synaptic Dysfunctions. *Angew. Chem., Int. Ed.* **2012**, *51*, 1576−1579.

DOI: 10.1021/acs.jpcb.9b04208
J. Phys. Chem. B XXXX, XXX, XXX−XXX

(110) Rosenman, D. J.; Connors, C. R.; Chen, W.; Wang, C.; García, A. E. Aβ Monomers Transiently Sample Oligomer and Fibril-Like Configurations: Ensemble Characterization Using a Combined MD/NMR Approach. *J. Mol. Biol.* **2013**, *425*, 3338−3359.
(111) Ball, K. A.; Phillips, A. H.; Wemmer, D. E.; Head-Gordon, T. Differences in β-strand Populations of Monomeric Aβ40 and Aβ42. *Biophys. J.* **2013**, *104*, 2714−2724.
(112) Ahmed, M.; Davis, J.; Aucoin, D.; Sato, T.; Ahuja, S.; Aimoto, S.; Elliott, J. I.; Van Nostrand, W. E.; Smith, S. O. Structural conversion of neurotoxic amyloid-β1-42 oligomers to fibrils. *Nat. Struct. Mol. Biol.* **2010**, *17*, 561.
(113) Huy, P. D. Q.; Vuong, Q. V.; La Penna, G.; Faller, P.; Li, M. S. Impact of Cu(II) Binding on Structures and Dynamics of Aβ42 Monomer and Dimer: Molecular Dynamics Study. *ACS Chem. Neurosci.* **2016**, *7*, 1348−1363.
(114) Streltsov, V. A.; Varghese, J. N.; Masters, C. L.; Nuttall, S. D. Crystal Structure of the Amyloid- p3 Fragment Provides a Model for Oligomer Formation in Alzheimer's Disease. *J. Neurosci.* **2011**, *31*, 1419−1426.
(115) Bernstein, S. L.; Dupuis, N. F.; Lazo, N. D.; Wyttenbach, T.; Condron, M. M.; Bitan, G.; Teplow, D. B.; Shea, J.-E.; Ruotolo, B. T.; Robinson, C. V.; Bowers, M. T. Amyloid-β protein oligomerization and the importance of tetramers and dodecamers in the aetiology of Alzheimer's disease. *Nat. Chem.* **2009**, *1*, 326−331.
(116) Zheng, X.; Liu, D.; Roychaudhuri, R.; Teplow, D. B.; Bowers, M. T. Amyloid β-Protein Assembly: Differential Effects of the Protective A2T Mutation and Recessive A2V Familial Alzheimer's Disease Mutation. *ACS Chem. Neurosci.* **2015**, *6*, 1732−1740.
(117) Urbanc, B.; Betnel, M.; Cruz, L.; Bitan, G.; Teplow, D. B. Elucidation of Amyloid β-Protein Oligomerization Mechanisms: Discrete Molecular Dynamics Study. *J. Am. Chem. Soc.* **2010**, *132*, 4266−4280.
(118) Gu, L.; Liu, C.; Stroud, J. C.; Ngo, S.; Jiang, L.; Guo, Z. Antiparallel Triple-Strand Architecture for Prefibrillar Aβ42 Oligomers. *J. Biol. Chem.* **2014**, *289*, 27300.
(119) Pan, J.; Han, J.; Borchers, C. H.; Konermann, L. Conformer-Specific Hydrogen Exchange Analysis of Aβ(1-42) Oligomers by Top-Down Electron Capture Dissociation Mass Spectrometry. *Anal. Chem.* **2011**, *83*, 5386−5393.
(120) Reddy, G.; Straub, J. E.; Thirumalai, D. Dry Amyloid Fibril Assembly in a Yeast Prion Peptide Is Mediated by Long-Lived Structures Containing Water Wires. *Proc. Natl. Acad. Sci. U.S.A.* **2010**, *107*, 21459−21464.
(121) Rangachari, V.; Moore, B. D.; Reed, D. K.; Sonoda, L. K.; Bridges, A. W.; Conboy, E.; Hartigan, D.; Rosenberry, T. L. Amyloid-β(1−42) Rapidly Forms Protofibrils and Oligomers by Distinct Pathways in Low Concentrations of Sodium Dodecylsulfate†. *Biochemistry* **2007**, *46*, 12451−12462.
(122) Terzi, E.; Hölzemann, G.; Seelig, J. Interaction of Alzheimer β-Amyloid Peptide(1−40) with Lipid Membranes†. *Biochemistry* **1997**, *36*, 14845−14852.
(123) Rangachari, V.; Dean, D. N.; Rana, P.; Vaidya, A.; Ghosh, P. Cause and consequence of Aβ - Lipid interactions in Alzheimer disease pathogenesis. *Biochim. Biophys. Acta, Biomembr.* **2018**, *1860*, 1652−1662.

DOI: 10.1021/acs.jpcb.9b04208
J. Phys. Chem. B XXXX, XXX, XXX−XXX